

Microfluidic Fabrication and Analysis of Biocompatible, Monodisperse DNA-Hydrogels with Tunable Swelling and Dissolution Kinetics

Corinna Torabi[#]

Department of Mechanical Engineering, Johns Hopkins University, Baltimore, Maryland 21218, USA

Takayuki Suzuki[#]

Department of Mechanical Engineering, Johns Hopkins University, Baltimore, Maryland 21218, USA

Emily Helm

Department of Chemistry, Johns Hopkins University, Baltimore, Maryland 21218, USA

Harrison Khoo

Department of Mechanical Engineering, Johns Hopkins University, Baltimore, Maryland 21218, USA

Sophie Tanengaum

Department of Biomedical Engineering, Johns Hopkins University, Baltimore, Maryland 21218, USA

Rebecca Schulman^{*}

Department of Chemical and Biomolecular Engineering, Johns Hopkins University, Baltimore, Maryland 21218, USA

Department of Computer Science, Johns Hopkins University, Baltimore, Maryland 21218, USA

Department of Chemistry, Johns Hopkins University, Baltimore, Maryland 21218, USA

Institute for NanoBioTechnology, Johns Hopkins University, Baltimore, Maryland 21218, USA

Soojung Claire Hur^{*}

Department of Mechanical Engineering, Johns Hopkins University, Baltimore, Maryland 21218, USA

Department of Oncology, Johns Hopkins University School of Medicine, Baltimore, Maryland 21218, USA

The Sidney Kimmel Comprehensive Cancer Center, Johns Hopkins Hospital, Baltimore, Maryland 21218, USA

Institute for NanoBioTechnology, Johns Hopkins University, Baltimore, Maryland 21218, USA

[#] Equal Contribution

^{*} Corresponding Authors

Abstract

Stimulus-responsive DNA-hydrogels with swelling capabilities are a promising class of materials for biomedical applications such as drug delivery and biosensing. Designing these systems remains challenging because fabrication methods must be simultaneously biocompatible and conserve scarce DNA materials, even at the microscale. Moreover, stimulus-induced swelling must be precisely controlled and shown to drive measurable changes in molecular properties. We present a biocompatible fabrication and characterization method for micron-scale DNA-hydrogels (μ SDs) with tunable isotropic swelling and dissolving properties. We first developed a fabrication method demonstrating that both the hydrogel composition and the fabrication process itself are biocompatible, while also minimizing the consumption of valuable DNA reagents. We then demonstrated modular control over isotropic swelling in micron-scale DNA microgels, achieving up to a two-fold size increase with tunable swelling through defined design parameters. We further established a quantitative workflow to measure structural changes of spherical, swollen and unswollen μ SDs leveraging the diffusive properties of a DNA-binding dye. Finally, we demonstrate tunable dissolving of μ SDs and quantitatively reveal various experimental factors that influence dissolution rates beyond what is traditionally considered in μ SD experiments. Together, these advances establish a biocompatible platform for the fabrication and analysis of stimulus-responsive DNA micro-hydrogels, providing a foundation for their future use in drug delivery, biosensing, and related biomedical technologies.

1. Introduction

DNA-hydrogels have attracted significant attention for various biomedical applications including tissue engineering [1], drug delivery [2–4], and bioprinting [1,5]. Their high-water content, intrinsic biocompatibility of DNA, and the natural degradability of DNA in the body make DNA-hydrogels especially suitable for biomedical applications [1]. Moreover, the programmability of DNA allows DNA-hydrogels to be tailored to mimic the mechanical properties of the extracellular matrix (ECM), supporting cell adhesion, growth, and immobilization [1,5,6].

With advances in nucleic acid engineering, DNA-hydrogels may now be further programmed, giving rise to a class of stimulus-responsive DNA-hydrogels (SRDHs) [7,8]. SRDHs harness the sequence-specific programmability of DNA to design hydrogels which undergo molecular or structural changes in response to external cues such as temperature [9], light [3,10], pH [4,11], ionic strength [12], or specific biomolecules [1,13–15]. The structural programmability of SRDHs enables precise tuning of mechanical properties to mimic specific ECM environments [10,16–18]. In addition, molecular changes enable tunable permeability that supports cell viability by facilitating nutrient and waste transport [16,18,19] or can be leveraged to deliver specific target molecules for detection applications [20]. SRDHs can also be

modulated to have precise dissolution rates enabling precise control over drug release profiles and programmable cell release, offering significant potential for applications in drug delivery and regenerative therapies [21–25].

Among various SRDHs, swellable SRDHs are particularly compelling for both detection and controlled transport of small molecules [20]. In swellable SRDHs, molecular DNA chains extend in the presence of a target molecule, to expand the polymer-DNA network, producing macroscopic swelling of the SRDH [26]. The resulting volume change can serve as a sensing readout indicating the presence of target molecule [7]. In addition, by controlling the degree of swelling, swellable SRDHs permit precise tuning of DNA-polymer network size without redesigning the underlying DNA, thereby optimizing nutrient transport and ECM-like structural properties for diverse cell applications. Taken together, these capabilities highlight how swellable SRDHs translate molecular recognition into diverse biomedical functions, enabling versatile applications in sensing and tissue engineering.

To fully exploit these functions in biological contexts, however, SRDHs should operate at length scales comparable to cells and tissues. For example, in drug delivery applications, it is often essential for SRDHs to be micron to sub-micron scale as their size directly influences the specific site of delivery [27,28]. Micron-sized hydrogels are particularly advantageous because their reduced dimensions shorten diffusion distances, accelerate swelling responses, and match the size regime of individual cells, thereby improving both sensitivity and biocompatibility.

A critical next step in translating SRDHs into practical tools is therefore the ability to fabricate them at the micron scale while maintaining both biocompatibility and stimulus responsiveness. For microscale studies, such as molecular diffusion or single-cell assays, micron-sized hydrogels reduce material requirements [29], enhance analyte transport [30,31], and increase sensitivity to subtle concentration changes [20,32]. Several strategies have been explored for producing micron-scale SRDHs, including UV patterning [7,10], which allows complex architectures but induces phototoxicity that limits use for live-cell applications [33]. Likewise, crosslinking approaches triggered by pH or temperature are often unsuitable for sensitive cells [34]. In contrast, microfluidic droplet generators provide precise control and reproducibility, yielding biocompatible, monodisperse DNA-hydrogel microgels [35,36] without cytotoxic triggers.

Once fabricated, micron-sized hydrogels also present unique challenges that must be addressed, particularly concerning the measurement of their molecular structure. Due to the reduced diffusion distance in these hydrogels, molecular transport properties (diffusion) are influenced not only by the pore size of the DNA-polymer network but also by the geometry of the particles [37]. For instance, particles with rectangular or square shapes may exhibit distinct diffusion behavior at their corners and edges [37]. Additionally, the soft and delicate nature of DNA-hydrogels complicates traditional measurement techniques [20,38–40]; methods like cryo-scanning electron microscopy (cryo-SEM), which rely on rapid freezing to preserve hydrogel structures, can inadvertently damage the material [41,42]. Although gentle methods, such as measuring diffusion induced transport across the material to infer molecular structure [43–46] may be applied to DNA-hydrogels [16,20], these techniques typically require hydrogels to be formed into sheet structures, rendering them incompatible with measuring geometry-dependent diffusion. While there are methods available that allow for the measurement of porosity in free-standing (non-sheet-like, dome shaped) hydrogels [41], these necessitate single-molecule tracking capabilities and to our knowledge have not been adapted for micron-scale DNA-hydrogels. Therefore, to enhance the application of micron-scale DNA-hydrogels, it is essential to develop gentle approaches for assessing molecular structural changes that are geometry-independent and do not require specialized equipment.

In this work, we advance droplet microfluidic fabrication of micron-scale SRDHs (μ SDs) on multiple fronts. We improved upon earlier swellable DNA-polymer networks [26] by replacing conventional polymers with biocompatible materials and redesigning the DNA sequences to achieve our current architecture. Using these materials, we developed a minimal-loss fabrication protocol for generating monodisperse μ SDs, improving scalability while reducing material waste. We validated the biocompatibility of both the fabrication protocol and DNA-polymer network by encapsulating cells and confirming their viability. We further demonstrated that the hydrogels preserved stimulus responsiveness at the micron scale, enabling modular control of isotropic swelling and achieving greater final expansion than previously reported at micron scale [7,35]. We also established a data-driven workflow to quantify the swelling induced changes in molecular structures by comparing the diffusive properties of a DNA binding fluorescent molecule into swollen and unswelled hydrogels. While diffusion approaches typically utilize a non-reactive molecule to simplify analysis [44–46], our method employs a reactive material. This innovation allows us to indirectly derive the diffusion of the free-floating YOYO-1 from the fluorescence emitted by the DNA bound (immobilized) YOYO-1, eliminating the need for challenging single-molecule tracking [47] or other specialized equipment [41]. Our approach offers a scalable, versatile method to measure molecular structural changes in μ SDs, including for applications that require specific particle sizes and complex geometries [34]. Finally, we designed a DNA strand to induce the structural breakdown of μ SDs and quantitatively demonstrate the breakdown can be modulated by adjusting the dissolving strand concentration. While DNA dissolution characterizations are often conducted in confined environments such as 1.5 mL tubes [21–25], we highlight the importance of considering diffusion kinetics in more complex experimental conditions, as dissolution rates can vary significantly between confined and non-confined systems. Collectively, these advances establish a robust, biocompatible platform for fabricating and analyzing μ SDs at the microscale, opening opportunities in drug delivery, biosensing, and single-cell studies within uniform hydrogel compartments.

2. Materials and Methods

2.1. Microfluidic device design and fabrication

A three-inlet microfluidic flow focusing droplet generation device was designed to handle two aqueous hydrogel precursor solutions (dispersed phase) as well as a continuous oil phase. The flow focusing channel geometry is illustrated in Figure S1a. The length of the initial dispersed phase channel was 25 mm and the width is 40 μ m. At the first T-junction, pregel-1 (containing cells) and pregel-2 flow in parallel. This co-flow breaks into droplets at the second T-junction. The distance between two T-junctions was 120 μ m (width of 40 μ m). After the second junction, the channel opens into a triangular region for droplet formation, followed by a 64 μ m channel to the outlet. Channel geometry was created with AutoCAD (Autodesk) software and a corresponding photomask was printed (ArtNet Pro, Inc.). The device was fabricated by soft lithography. A negative photoresist (KMPR 1035, Kayaku Materials) was spin coated onto a silicon wafer (University Wafers) to achieve the desired height (60 μ m), followed by baking at 100°C for 15 minutes. The photoresist was patterned by UV exposure through the using a mask aligner (EVG620). Uncured photoresist was removed by washing with SU-8 developer (Kayaku Materials) for 3–5

minutes, after which the wafer was hard baked at 200°C for 20 minutes. The mold height ($61.3 \pm 0.05 \mu\text{m}$) was confirmed using surface profilometer measurements at 4 locations (Keyence VK X250).

The channel structure was created by casting poly(dimethylsiloxane) (PDMS; Sylgard 184, Dow Corning) over the mold mixed a ratio of 10:1 elastomer and curing agent. The PDMS was degassed under vacuum for at least 10 minutes to remove air bubbles and then cured overnight at 70°C. Cured PDMS was cut into individual devices, and inlet/outlet holes were punched (Pin Vise Set A and Set C, Syneo). PDMS devices were bonded to clean glass slides (Histobond Supa Mega Slides, cat# 71881-60, Electron Microscopy Sciences) using O₂ plasma treatment (Atto Plasma Cleaner, Diener Electronic) at 75 W for 75 seconds. Bonded devices were rested at least 24 hours before use to reduce undesirable hydrophilic effects of plasma treatment, which prevents the oil phase from properly dispersing the aqueous phase into droplets due to the aqueous phase wetting the droplet generation junction.

2.2. Preparation of micron-scale DNA-crosslinked hydrogel (μSD)

DNA-crosslinked hydrogels were prepared by reconstituting all DNA components in nuclease-free water. S1-C (pre-gel 1) and S1-C' (pre-gel 2) pre-gels were formulated separately by combining 1.2x PBS (pH 7.4, Cat# 119-069-131, Quality Biological), 4% acrylamide solution (A4058, Sigma-Aldrich), 1.8mM of respective 5'-acrydite-modified oligonucleotide (S1-C or S1-C'; IDT), and a 5'-acrydite-modified Poly-T Cy3 oligonucleotide (IDT). After vortexing and brief centrifugation, polymerization was initiated by adding 2.5% (v/v) TEMED (T9281, Sigma-Aldrich) and 0.5% (w/v) ammonium persulfate (APS, ref. 17874, Sigma-Aldrich), and the mixtures were incubated at room temperature for 15 minutes. The resulting viscous pre-gels were then degassed under vacuum in a desiccator for an additional 15 minutes. To assemble the DNA-crosslinked hydrogel in bulk, equal volumes of pre-gel 1 and pre-gel 2 were combined using a positive displacement pipette with 1 μL of 1x PBS added per 5 μL each pre-gel, and the mixture was allowed to gel at room temperature. A complete list of oligonucleotide sequences is provided in Table 1.

Table 1: Sequence of DNA strands used in this study.

Strand	[Stock] in water	Sequence (5'-3')
Poly(10)-T-Cy3	100 μM	/5Acryd/TTTTTTTTTT/3Cy38p/
S1-C	3 mM	/5Acryd/TAAGTCGCTGTGGCACCTGCACGG
S1-C'	3 mM	/5Acryd/CAACGTGCAGGTGCCACAGCGTGG
Hairpin 1 (H1)	770 μM	CCACGCTGTGGCACCTGCACGCACCCA CGTGCAGGTGCCACAGCGAACTTA
Hairpin 2 (H2)	650 μM	TGGGTGCGTGCAGGTGCCACAGCGTAAGTT CGCTGTGGCACCTGCACGTTG
H1 terminator (H1term)	160 μM	CCACGCTGTGGCACCTGCACGTAGACT CGTGCAGGTGCCACAGCGAACTTA
H2 terminator (H2 term)	134 μM	TGGGTGCGTGCAGGTGCCACAGCG GCCTAGCGCTGTGGCACCTGCACGTTG
Dissolver (DS)	300 μM	CGTGCAGGTGCCACAGCGAACTTA
Dummy-24nt (d-24)		GGTCTCCTCTGCTTAGGAGACTT

2.3. Microfluidic μSD production and recovery

Prior to droplet generation, the microfluidic channels were filled with a hydrophobic glass coating (Rain-X) and incubated for 10 minutes. The coating solution was then removed from the channels by withdrawing it with a syringe. This step increased channel-wall hydrophobicity, enhancing droplet generation consistency by preventing the adhesion of the dispersed aqueous phase to the channel walls. The adhesion of the aqueous phase at the droplet generation junction and outlet channel prevents consistent dispersion of droplets and causes the crosslinked hydrogel to build up and block in the outlet channel over time. Channels were next pre-wetted with oil by filling them with HFE7500 oil (RAN Biotechnologies), which further minimized the adhesion of the aqueous phase in droplet generation junction and outlet channel.

Three distinct solutions were prepared for injection into the three-inlet flow focusing droplet generator. Two hydrogel precursor solutions, pre-gel 1 and pre-gel 2, were separately prepared in tubes to prevent premature crosslinking of the μSDs . Pre-gel 1 was diluted 2-fold in DPBS (with Ca²⁺ and Mg²⁺, 14040133, Gibco) due to its high starting viscosity making it incompatible with the restricted flow in the microfluidic channel. When applicable, the K562-F cells were suspended in pre-gel-1 at a concentration of 5×10^6 cells/mL. To efficiently utilize small hydrogel volumes ($\leq 100 \mu\text{L}$), we adapted a small-volume loading workflow described by Sinha *et al.* [48]. Briefly, a 5-mm diameter PDMS disc approximately 10 mm thick was created using a biopsy punch (5 mm Harris Uni-Core, 15081), and a central hole matching the outer diameter of the Tygon ND 100-80 tubing (outer diameter 0.06 in, AAD04103, Saint Gobain) was punched using a pin vise. The PDMS disc was then fitted onto a 200 μL pipette tip (1111-706, USA Scientific) and connected via the Tygon tubing to a 1 mL plastic syringe (309628, BD Medical) pre-filled with inert paraffin (mineral) oil (PC5530, Bio Basic). The pipette tip was filled with mineral oil from the syringe and then the hydrogel pre-gel solution was loaded into the pipette tip by withdrawing the syringe.

HFE7500 oil with 2% FluoroSurfactant (RAN Biotechnologies) was loaded into a 5 mL syringe (309646, BD Medical) and fitted with PEEK tubing (1569, IDEX). Programmable infuse/withdraw syringe pumps (two PHD Ultra, Harvard Apparatus; one Legato, KD Scientific) independently controlled inlet flow rates: 30 $\mu\text{L}/\text{hr}$ for pre-gel 1, 8 $\mu\text{L}/\text{hr}$ for pre-gel 2, and 425 $\mu\text{L}/\text{hr}$ for oil with surfactant. The setup of the experimental components and the data collection tools included multiple components to achieve reliable, real-time monitoring of droplet generation. A high-speed camera (Phantom v2012, Vision Research, Inc) and accompanying high power light source (SOLIS-3C, THORLABS) was connected to the microscope to enable high-speed video capture of the droplet generation. Videos were recorded at 5,000 to 10,000 frames per second.

Droplets were collected in a 1000 μ L pipette tip fitted into the outlet hole to collect μ SDs with minimal aggregation. The carrier oil containing crosslinked μ SDs was transferred from the collection pipette tip into a microcentrifuge tube for demulsification [49]. Approximately 100 μ L of DPBS (with Ca^{2+} and Mg^{2+} , cat#14040133, Gibco) was added as the aqueous phase, and after allowing clear phase separation, ~90% of oil phase was carefully removed from the bottom of the tube using a pipette. To break the remaining emulsion, fresh HFE7500 oil containing 20%(v/v) 1H,1H,2H,2H-perfluorooctanol (PFO, 370533, Sigma-Aldrich) was added to the μ SDs and gently mixed with a pipette. Once the oil and aqueous layers re-separated, the μ SDs were partitioned into the DPBS. This demulsification process was repeated once or twice more until no emulsified oil remained. After a final 10-minute settling, the residual oil phase was fully removed, leaving purified μ SDs in DPBS. For non-cellular assays, the μ SDs were stored at 4°C; for viability tests, they were immediately plated in 12-well or 96-well plates with complete cell culture media and incubated at 37°C. Media exchanges were performed by centrifuging the well plate at 150 x g for 1 minute, leaving just enough liquid to prevent μ SD loss.

2.4. Cell culture

Human lymphoblasts K562-FUCCI (K562-F) cells were encapsulated into hydrogel microparticles via droplet generation. K562-F cells were produced by introducing fluorescence ubiquitination cell-cycle indicator (FUCCI) constructs [50] into K562 cells (CLL-243™, ATCC) using lentiviral transduction. Lentiviral vectors were generated by transiently transfecting HEK293T/17 cells (CLR-11268, ATCC) with plasmids encoding the FUCCI reporters mKO2-hCdt1(30/120)/pCSSII-EF-MCS and mAG-hGeminin(1/110)/pCSSII-EF-MCS, along with the lentiviral envelope plasmid pCMV-VSV-G-RSV-Rev and packaging plasmid pCAG-HIVgp. The resulting lentiviruses encoded fluorescent proteins (monomeric Kusabira Orange 2, mKO2; monomeric Azami Green, mAG) fused to cell cycle-specific degrons derived from human Cdt1 and Geminin proteins, respectively. FUCCI-related plasmids, including the lentiviral constructs, packaging, and envelope vectors, were generously provided by Dr. Atsushi Miyawaki (RIKEN Institute, Japan). Post-transduction, K562-F cells were sorted by fluorescence-activated cell sorting (MoFlo Astrios Cell Sorter, Beckman Coulter Life Sciences) to select populations simultaneously expressing both mAG and mKO2 fluorescent signals. Sorted cells were cultured in IMDM (cat#12440053, Gibco) supplemented with 10% FBS (cat#10082147, Gibco), 1% Penicillin-Streptomycin (cat#15070063, Gibco), and 0.1% gentamycin sulfate (cat#15750060, Gibco) at 37°C in a humidified incubator with 5% CO_2 . Prior to encapsulation, cells were washed in fresh serum-free IMDM and filtered through a 40 μ m pipette tip filter (H136800040, Flowmi, Bel-Art) to minimize clumping of cells during experiment. K562-F cells at a concentration of 5×10^6 cells/mL were pelleted and re-suspended in 150 μ L of pregel-1.

2.5. Cell viability assessment

Cell viability was assessed after microfluidic cell encapsulation in μ SD microparticles and subsequent washing of microparticles to remove oil phase. Cells from the same flask that were not passed through the device served as control counterparts and were processed in parallel. Both control and encapsulated cells were suspended in 1 μ M Calcein Blue, AM (Invitrogen, C1429) in DPBS and incubated for 30 minutes at 37°C. Due to high DNA concentration in the hydrogel, cells could not be assessed with DNA binding molecules as the signal from the hydrogel network would interfere with the cell signal. Rather, cell nuclei were identified by the FUCCI reporter, and viability was calculated as the fraction of cells positive for both the FUCCI signal and Calcein Blue fluorescence. Imaging was performed on an inverted microscope (Eclipse Ti2, Nikon Inc., Japan) equipped with a white light source (Sola Light Engine, Lumencor) and filter cubes capable of fluorescence imaging, and a CCD camera (CoolSNAP DYNQ, Photometrics).

2.6. μ SD swelling

To induce swelling, μ SDs (50 -100 per well) were dispersed into a clear-bottom 96-well plate (3694, Corning) and incubated with DNA hairpins (sequences in Table 1) at a final concentration of 20 μ M to extend the crosslinks and drive swelling [8]. To modulate the swelling kinetics, hairpin terminators (sequences in Table 1) were each tested separately at 0 μ M, 2 μ M, 5 μ M, 10 μ M, and 20 μ M, with each concentration in its own well. Swelling was continuously monitored on an inverted microscope (Eclipse Ti2, Nikon) equipped with a mercury Epi-fluorescent filter cube sets, and a CCD camera (Clara, Andor, USA) at room temperature, acquiring images once per every hour over a 24 h period using automated multi-point captures (NIS-Elements, Nikon Inc., Japan). μ SD dimensions were quantified from the red-fluorescence images.

Images of swelling μ SDs were analyzed using custom MATLAB scripts designed to robustly segment μ SD boundaries, accounting for imaging artifacts such as edge ridges and signal heterogeneity associated with swelling. Initial preprocessing was performed on the brightfield (BF) images to distinguish the interior of the well from the background. μ SD-associated fluorescence signal was then isolated by thresholding based on the mean intensity plus a standard deviation of intensity in the image. This was followed by a sequence of morphological operations including area filtering, smoothing, watershed segmentation, and hole filling to generate an approximate mask of each μ SD. At later time points (>15-20 h), some μ SDs fragmented, and others showed increased dark regions (ridges) due to reduced internal signal intensity, complicating segmentation. To mitigate these effects, we applied additional quality control filters: objects with an aspect ratio (AR) greater than 1.2, circularity less than 0.8, or classified as statistical outliers at each time point were excluded. After filtering, we retained over 30 μ SDs per time point for up to 17 hours, with an average of 90-200 μ SDs per time point across all experimental conditions. To further ensure segmentation quality, outlines of all detected μ SDs were visually reviewed in composite overlay images. For each segmented μ SD, we computed the radial diameter as a function of polar angle (θ), from which the average diameter was obtained.

2.7. Hydrogel molecular diffusion measurements

The effects of swelling on the porosity of the hydrogel crosslinking network were measured by imaging the fluorescence intensity of fluorescent molecule diffusing into the hydrogel microparticles. About 10-20 μ SDs were added to a well and located with a confocal microscope (10X, red-fluorescence channel, Four-Channel Confocal System, ThorLabs). A YOYO-1 nucleic acid stain (Y3601, Invitrogen) with a molecular weight of 1271 g/mol was added to each well at a final concentration of 1 μ M. Timelapse imaging captured the middle plane

slice of μ SDs every 5 seconds for 2 hours to measure the change in fluorescence intensity in the μ SDs as the fluorescent DNA stain bound to the DNA-crosslinking hydrogel structure.

Diffusion of YOYO-1 into our μ SDs was measured using confocal microscopy at 5-second intervals over a 120-minute period. To identify μ SDs for analysis, we first applied a thresholding algorithm similar to that described in Section 2.6 to segment and outline all visible structures. From these, we manually selected individual μ SDs that were circular, free of defects, and not in contact with neighboring μ SDs. The center and radius of each selected μ SD were recorded based on the geometric center of the circular diameter profile, $D(\theta)$ rather than the center of the segmentation mask. This choice minimized the influence of edge detection artifacts. Image analysis began at 10 minutes, after which the μ SDs generally remained static in the field of view. To account for minor shifts in highly swollen μ SDs after 10 minutes, the center location was updated at each time point. Early time points in the video had low signal-to-noise ratios (SNR), which made thresholding and analysis challenging. However, we observed that μ SDs did not drift more than 20% of their radius from their original position after 10 minutes. If a tracked center deviated beyond this threshold, the original barcoded center was used instead as the newly detected center was likely an error in detection. This algorithm enabled us to stabilize the minor shifts of μ SDs. At each time point, fluorescence intensity was quantified within a circular region defined by the frame specific center and initial radius. Intensity profiles were smoothed using MATLAB's 'smooth data' function with a Gaussian kernel with kernel width no greater than 3. The resulting intensity data were then used to fit a reaction-diffusion model, as described in the results section 3.3. For select plots we used MATLAB's built in function `smoothdata()` and an exaggerated 'gaussian' window 500 to plot noise-free general trend only for visualization purposes.

2.8. Hydrogel dissolving measurements

The hydrogel particles are dissolved by the Dissolver Strand (DS, sequence in Table 1) which disrupts the hybridization of the DNA crosslinks via a strand displacement reaction. DS is the full complement to C and is designed to be able to dissolve both unswelled and swollen gels can be dissolved with the same strand. DS dissolves unswelled particles by binding to a three-nucleotide length single-stranded region (the toehold) on C in the C:C' duplex and then displacing C', thereby disrupting the gel matrix. In swollen particles, H1 is also complementary to C, leaving no single-stranded region that can act as a toehold for dissolution. DS mainly dissolves swollen particles by instead binding to a six-nucleotide length single-stranded region on H2, separating C' from the hybridization chain through strand displacement. If DS is added in excess, a small amount of dissolution can occur by DS successfully competing with H1 for binding to C, as H1 will be driven to bind to itself, returning to a hairpin. We validated our dissolving mechanism using PAGE (Figure S7). We also designed a dummy DNA oligo to confirm that simply adding excess DNA is not the cause of hydrogel dissolution. We designed and analyzed a 24 nucleotide DNA oligo (d-24) using NUPACK [51] to validate the lack of secondary structure. This strand is used in particle dissolving experiments as a control for DS.

Unswelled μ SDs were dispersed in a clear, flat-bottom, half-area 96-well plate (3696, Corning) and incubated with the DS (Table 1) at varying concentrations to induce the dissolution of DNA-crosslinked hydrogels. DS concentrations of 0, 0.5, 1, 2, and 4 μ M were tested in separate wells to modulate dissolution kinetics. Dissolution was monitored continuously using an inverted microscope (Eclipse Ti, Nikon Inc., Japan) equipped with a mercury lamp and epi-fluorescent filter cube sets and a CCD camera (Clara, Andor, USA). Images were captured at room temperature at 2-minute intervals for the 4 μ M condition and at 10-minute intervals for all other concentrations, using an automated multi-point capture system (NIS-Elements, Nikon Inc., Japan). The half-area well plate with a reduced footprint was required to continuously image all the wells within the desired time interval. Red-fluorescent images, corresponding to Cy3-labeled polyacrylamide, were acquired to quantify hydrogel dimensions and the fluorescence intensity associated with remaining polymer during dissolution [52]. Dissolution data were analyzed using custom MATLAB scripts adapted from the μ SD swelling analysis pipeline (section 2.6), enabling segmentation of μ SDs and quantification of fluorescence intensity over time.

3. Results and Discussion

In this work, we developed a droplet microfluidic platform for producing, monodisperse, biocompatible, micron-sized, stimulus-responsive μ SDs with minimal material loss (Figure 1). This system enables reproducible fabrication of uniform μ SDs, supports live-cell encapsulation, and preserves stimulus responsiveness with tunable swelling kinetics. We further used diffusion kinetics to probe network sparseness, establishing μ SDs as a robust platform for cell-compatible, modular hydrogel studies. Finally, we demonstrate that the dissolving rates of μ SDs can be modulated while emphasizing the often-overlooked effects of confined versus unconfined experimental conditions.

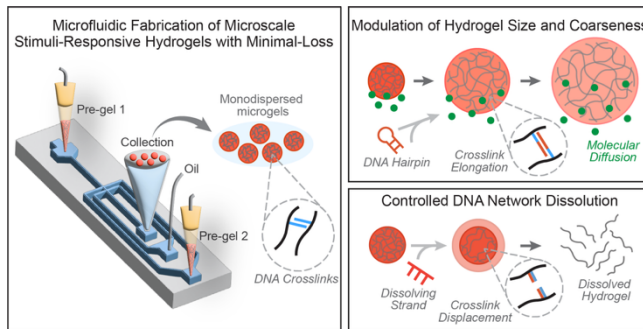


Figure 1: Overview of process for fabricating microscale stimuli-responsive μ SDs and swelling and dissolving of μ SDs.

3.1. Material-efficient fabrication and validation of monodisperse μ SDs

We used microfluidic droplet generation to produce monodisperse, micron-sized, DNA-crosslinked hydrogels (μ SDs) that offer precise control over size, composition, and responsiveness. Microscale, monodisperse hydrogels provide uniform environments for studying molecular diffusion, stimulus-induced swelling, and single-cell encapsulation, where consistent particle size and composition are essential for reproducibility. The ability to program μ SDs at this scale enables systematic investigation of structure-function relationships and facilitates integration with microscale analytical systems.

To implement this, we designed a droplet microfluidic system capable of forming DNA-crosslinked hydrogel microparticles with precise control over crosslinking initiation. Because hydrogel formation initiates immediately when the two complementary DNA strands – each conjugated in separate pre-gel solutions (pre-gel 1 with S1-C and pre-gel 2 with S1-C' Figure 2a,b) – come into contact, the device required additional precautions compared with standard water-in-oil emulsions. To ensure simultaneous merging of the two pre-gel streams and droplet pinch-off, we used a three-inlet microfluidic device (Figure 2c) that introduces the two pre-gel streams independently. They converge only at the droplet junction, where the oil carrier phase shears the flow into discrete aqueous droplets that rapidly crosslink into uniform hydrogel microparticles.

Compositional precision in DNA-crosslinked hydrogels demands small working volumes, motivating the development of a material-efficient droplet generation system and workflow compatible with other small-volume. While microfluidic systems are well suited for handling small volumes, syringe and tubing setups typically include regions of unusable ‘dead’ volume. For example, the tip of a 1 mL syringe (\sim 70 μ L) and 10 inches of PEEK tubing with a 0.02-inch inner diameter (\sim 51.5 μ L) together contribute over 100 μ L of dead volume, greater than the 100 μ L starting volume of our pre-gel solutions, making this setup impractical. In contrast, the internal volume of each pre-gel inlet channel leading to the droplet junction was only \sim 0.061 μ L, highlighting the most material loss arises from the external delivery system rather than the microfluidic device itself. To address this, we adapted a method that uses mineral oil to drive the flow of the small volume fluid through a pipette tip attached to the typical syringe setup, effectively filling the dead volume with mineral oil rather than hydrogel materials (Figure S1c) [48]. The pre-gel solutions were loaded exclusively in 200 μ L pipette tips, filling the lower part of the tip while the lighter mineral oil remained above the pre-gel. The flow was stopped when the pre-gel volume reached the height of the microfluidic device (\sim 6 mm) and the was visually obscured by the PDMS, leaving about 4-5 μ L of pre-gel left, assuming an average pipette tip inner diameter of 1 mm. Stopping the flow before the oil phase above the pre-gel is reached is necessary to prevent microdroplets containing only one pre-gel from forming while also preventing from surfactant free mineral oil mixing with the collected droplets. This pipette tip technique enables the usage of $>95\%$ for a maximum starting volume of 100 μ L, whereas a conventional setup using syringes and tubing prohibits the usage of such small volume due to the >100 μ L dead volume in the system.

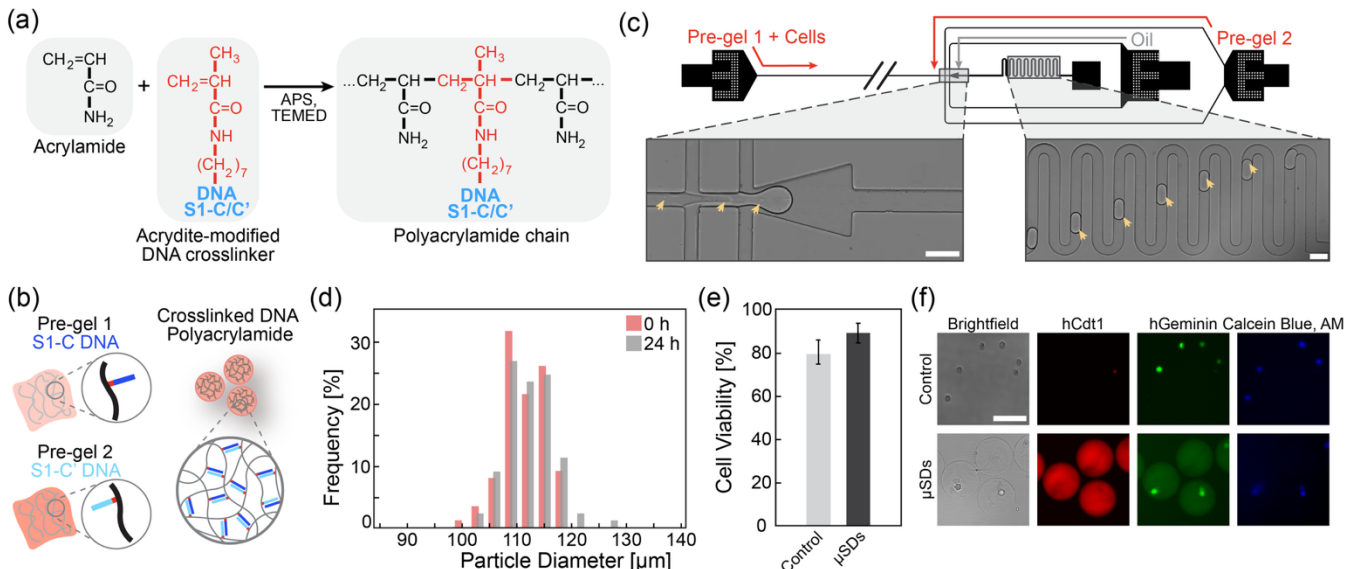
After minimizing losses at the inlets, we next addressed material loss at the outlet of the microfluidic system. The use of a typical configuration, in which the outlet was connected to tubing leading to a collection microcentrifuge tube, resulted in noticeable loss of intact microparticles. During operation, some hydrogels aggregated within tubing and merged, occasionally obstructing the tubing and damaging outflowing particles. This aggregation likely arose from the substantially lower flow velocity within the larger-diameter outlet tubing and the arched orientation of the outlet tubing into the collection microcentrifuge tube, which required the relatively less dense particles to move against the density gradient of the heavier oil – an inherent challenge of interfacing microscale channels with macroscale collection systems. The outlet tubing also introduced additional dead volume at the end of each run. To eliminate these losses, we replaced the outlet tubing with a 1 mL pipette tip directly inserted into the outlet to collect the produced hydrogel microparticles and carrier oil. Combining this outlet modification with the inlet optimization maximized the usable pre-gel volume and minimized loss of successfully generated DNA-crosslinked hydrogel microparticles.

Droplet generation was assessed using high-speed imaging (Figure 2c). Droplets were generated at a rate of 16.8 droplets/second, producing approximately 91,000 droplets through the 90-minute duration of the experiment. The resulting hydrogel microparticles were measured after release from the oil phase, yielding an average diameter of 113.1 ± 3.8 μ m (Figure 2d). The analyzed population exhibited a coefficient of variation (CV) of 3.4%, confirming high monodispersity. To evaluate the structural robustness of the fabricated hydrogels, we assessed their short- and long-term stability under different buffer and temperature conditions. The size distribution of μ SDs after 24 h in DPBS with Ca^{2+} and Mg^{2+} at room temperature remained nearly identical to that measured immediately after fabrication (mean diameter of 113.8 ± 4.0 μ m, CV 3.5%), confirming consistent size retention and structural integrity (Figure 2d). When stored in the same buffer at 4°C for 15 weeks, the μ SDs exhibited no change in size, demonstrating utility as a long-term storage buffer.

We further tested μ SD stability in cell culture media to assess their response to biologically relevant degradation factors. At 4°C, μ SDs also remained stable for at least 24 h serum free IMDM (mean: 111.2 ± 3.5 , n=10) and complete culture medium (IMDM + 10% FBS + 1% antibiotics) (mean: 109.4 ± 2.5 , n=8) (Figure S2a). However, at 37°C in complete medium, the μ SDs increased in diameter by about 12% to 126.6 ± 4.7 μ m (n=9), indicating partial degradation, likely due to DNases activity present in FBS, which becomes more active at elevated temperatures. Adding a high concentration of 10 mM EDTA to the μ SDs in complete media showed no visual degradation of the μ SDs, confirming that DNase activity in the complete growth medium was responsible for particle degradation (Figure S2b). Because high levels of EDTA are not compatible with cell culture, these findings primarily demonstrate the role of DNase activity in hydrogel degradation rather than a practical preservation strategy.

To verify that our fabrication and washing protocol is compatible with living cells, we assessed the short-term biocompatibility of μ SDs and the microfluidic process using K562-FUCCI cells. The hydrogel microparticles were loaded with cells during microfluidic droplet generation. The full process, including sample preparation, droplet generation, and hydrogel droplet washing, required approximately 3 h. Encapsulated cells maintained viability compared to untreated control cell population (Figure 2e and f), confirming that the DNA-polymer network and the fabrication process are compatible with living cells.

Collectively, these findings demonstrate that μ SDs fabricated using our microfluidic platform are structurally stable across a range of buffer and temperature conditions while maintaining size and monodispersity after storage, highlighting the reproducibility, precision, and material efficiency of the fabrication process, which enables robust and predictable yield of uniform μ SDs for downstream functional analyses.



3.2. Programmable swelling kinetics and size regulation of μ SDs

The internal DNA architecture of our hydrogels enables precise modulation of swelling through programmable strand displacement reactions. Following the design of DNA polymerization gels by Fern *et al.*, swelling in our system is driven by hybridization chain reaction (HCR), where complementary DNA hairpins sequentially insert into duplex crosslinks within the DNA-polymer network [8]. This process extends the DNA crosslinks and increases the overall network volume. The extent and rate of swelling are modulated by introducing a defined fraction of terminator hairpins, which compete with polymerizing hairpins for the same binding domains but halt further extension once incorporated. This design provides predictable control over both the swelling kinetics and final expansion of the μ SDs.

To demonstrate programmable swelling, μ SDs were incubated for 24 h with 20 μ M of DNA hairpins, of which terminators were presented 0 μ M, 2 μ M, 5 μ M, 10 μ M, or 20 μ M – corresponding to 0%, 10%, 25%, 50%, and 100% of the hairpin concentration. Swelling kinetics were quantified using a custom MATLAB script that tracked μ SD diameter over 24 h (Figure 3a) with only geometrically symmetric μ SDs (aspect ratios ≤ 1.2 , circularity ≥ 0.8) included in the analysis. Despite this filtering, each condition contained 90-200 μ SDs per time point and more than 30 per group were maintained up to 16 hours, providing sufficient sample size for robust statistical comparison (Figure S3).

Visual inspection revealed distinct dark, line-like features within the μ SDs (Figure 3b), presumably corresponding to interfaces between pre-gel 1 and pre-gel 2 that contained different concentrations of a 5'-acrydite-modified poly-T-Cy3 oligonucleotide, as pre-gel 1 was diluted two-fold in DPBS to reduce viscosity and enable stable microfluidic flow. We refer to these dark regions as ridges hereafter (Figure 3b). These ridges, previously observed in similar systems, are thought to form due to rapid crosslinking at the interfaces of the two pre-gel solutions during μ SD synthesis in the microfluidic channels [35,49]. To quantify ridge formation, we analyzed the fluorescence intensity distribution of each μ SD and calculated skewness as a measure of asymmetry [53]. Initially, μ SDs exhibited primarily bright intensity profiles (negative skewness). As ridges developed, the intensity distributions shifted toward lower fluorescence values, reflected by an increase in skewness over time (Figure 3c). μ SDs with terminator concentrations (0-50%) exhibited increases in skewness, indicating accelerated ridge formation, while unswelled controls showed no change. In some cases, ridges serve as fracture lines where the μ SDs split immediately before complete dissolution (Figure 3b; Supplementary Video).

Despite ridge formation, μ SDs retained high circular symmetry and uniform diameter profiles throughout swelling, with structural breakup only immediately prior to dissolving at later stages. Across conditions, variation in angular diameter profiles, $D(\theta)$, remained low ($CV D(\theta) < 10\%$), confirming isotropic swelling behavior (Figure 3d). Notably, this isotropy persisted even as fluorescence skewness increased, indicating that ridge formation caused optical heterogeneity without affecting the geometric uniformity of swelling. These findings justify using average μ SD diameter, D , as a reliable metric for quantifying time-dependent total swelling.

Across all conditions except the 100% terminator group, μ SDs swelled at comparable rates during the first 7 h (Figure 3e) with narrow size distributions ($CV D < 10\%$, Figure 3f, Figure S3b). The 100% terminator condition exhibited a higher initial swelling rate followed by rapid dissolution, likely due to network instability under reduced ionic strength caused by the increased buffer volume at high terminator concentrations (Figure 3e) [37]. After 7 hours, swelling trajectories diverged across terminator concentrations, with higher terminator levels yielding smaller final sizes. Although variability increased modestly over time (Figure 3g), μ SD diameter distributions remained within a narrow range (CV of $D < 10\%$) up to 15 hours for 50% terminator condition and up to 19 hours for all other conditions (Figure S3b). Beyond 19 hours, the CV increased sharply (Figure S3b), primarily due to reduced particle counts caused by factors such as

ridge growth that produced uneven fluorescence intensity that reduced segmentation accuracy, particles being pushed out of the imaging field by adjacent swelling neighbors, and gradual dissolution of μ SDs.

Notably, μ SDs without terminator (0%) reached up to twice their initial diameter within 20-h (Figure 3e), representing a substantial swelling response compared to previously reported microscale μ SDs, which typically expand by only ~30% [7,35], and approaching the expansion observed in millimeter-scale systems that can reach up to ~265% [26]. This expanded swelling range broadens the accessible gradient of hydrogel expansion, allowing precise modulation of swelling behavior through the terminator-to-hairpin ratios. These results establish that the interplay between hairpins and terminators enables programmable control of swelling kinetics and final size, forming the basis of tunable, uniform expansion μ SDs.

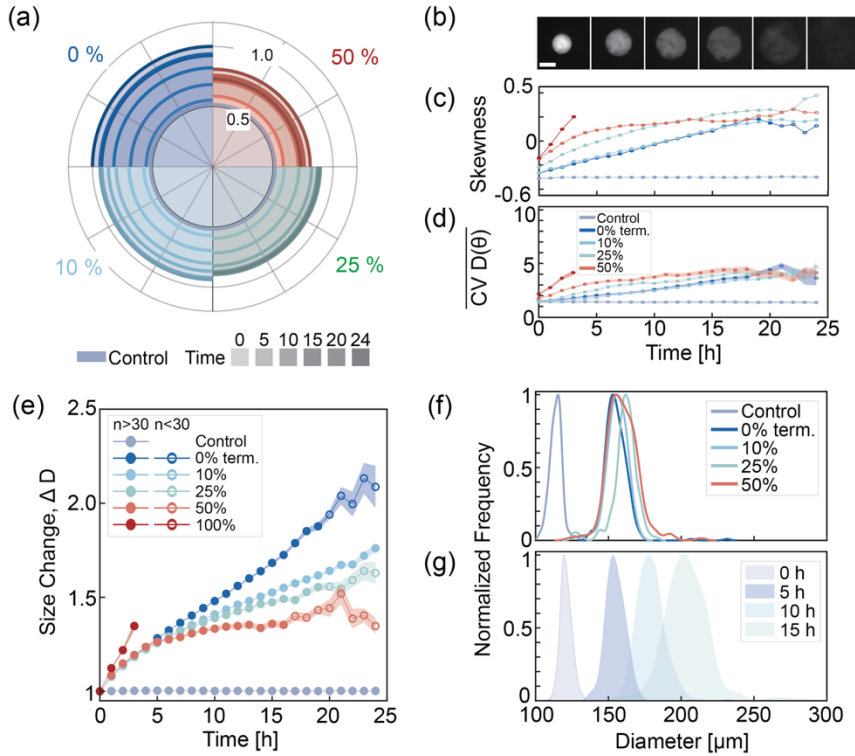


Figure 3: Swelling kinetics and microscale structural evolution of μ SDs. (a) Average diameter of μ SDs plotted in polar coordinates for 0, 10, 25, and 50% terminator at time points every 5 hours. Solid Blue circle represents average diameter of control μ SD. (b) Representative fluorescence microscopy images of a 0% terminator μ SD taken every 5 hours. Scale represents 100 μ m. (c) Skewness of μ SD intensity over time, reflecting the increasing prevalence of low-intensity regions (ridges) within the gel cross-section. Solid markers denote average values from a sample size greater than 30 μ SDs per time point (d) Coefficient of variation of diameter (CV D(θ)) as a measure of μ SD circularity across time points (e) Average change in diameter of μ SDs over time for varying terminator concentrations. Shaded regions represent standard error of the mean. (f) Distribution of μ SD sizes at time point 5 hours for terminator concentrations of 0%, 10%, 25%, and 50%. (g) Size distribution of μ SDs at 0% terminator across time 0, 5, 10, 15 hours showing temporal swelling progression.

3.3. Diffusion mediated characterization of swelling-induced network coarseness

Understanding molecular-level network changes due to swelling is key to establishing the structure-property relationships that govern permeability and diffusivity in μ SDs. While the previous section described programmable swelling at the microscale, the corresponding changes in polymer architecture warrant further assessment. Techniques such as SEM or microindentation can characterize morphology or bulk mechanics but are inadequate for resolving polymer network architecture in hydrated μ SDs, where dehydration or mechanical contact can disrupt the native structure. To address this, we leveraged the molecular accessibility of DNA linkers within the hydrogel, which allows penetration of small nucleic-acid-binding molecules. Using the intercalating dye YOYO-1 as a molecular tracer, we quantified diffusion kinetics to infer network coarseness in unswelled and swollen hydrogels (2 h and 5 h without terminators). This diffusion-based approach provides an *in situ*, non-destructive means to evaluate molecular-scale permeability changes accompanying hydrogel swelling. We captured time-lapse fluorescence images reflecting YOYO-1 binding dynamics during its diffusion into μ SDs every 5 s for 2 h. Due to the high affinity of YOYO-1 for DNA [54], the reaction was assumed to be rapid and diffusion-limited (Figure 4a). The probability of YOYO-1 binding depends on hydrogel porosity, local DNA concentration, and the available YOYO-1 concentration. This diffusion process can be modeled using a conventional reaction-diffusion framework:

$$\frac{\partial C_f}{\partial t} - \frac{\partial C_b}{\partial t} = D_{eff} \cdot \left(\frac{\partial^2 C_f}{\partial r^2} + \left(\frac{2}{r} \right) \cdot \frac{\partial C_f}{\partial r} \right) \quad (1)$$

$\frac{\partial C_f}{\partial t} = D_{eff} \cdot \left(\frac{\partial^2 C_f}{\partial r^2} + \left(\frac{2}{r} \right) \cdot \frac{\partial C_f}{\partial r} \right)$ represents Fick's second law of diffusion in spherical coordinates, where C_f is free YOYO-1, D_{eff} is the diffusion coefficient, and r is the distance from the hydrogel core [55]. The term $\frac{\partial C_b}{\partial t}$ accounts for the YOYO-1 immobilization via its reaction with DNA in the hydrogel network.

The binding of YOYO-1 to DNA can be described by a standard reaction model:

$$\frac{\partial C_b}{\partial t} = k_b \cdot C_f \cdot (\rho_o(r) - C_b) \quad (2)$$

where k_b is the reaction constant of YOYO-1, ρ_o is the total DNA concentration (binding sites) as a function of radius, and C_b is the bound YOYO-1. Thus, $\rho_o - C_b$ represents the change in available binding sites (unbound DNA) over time and radial position. The bound YOYO-1 is proportional to observed fluorescence intensity, $I(r, t) = \alpha \cdot C_b$, where α is a proportionality constant.

To ensure accurate application of the diffusion model, several analytical assumptions and constraints were imposed. First, the outer 5 μm of each hydrogel was omitted from spatial analysis to minimize edge-detection artifacts that could distort porosity-dependent diffusion estimation. Additionally, because hydrogels often moved in and out of the imaging field immediately after YOYO-1 introduction, likely due to transient fluid motion caused by pipetting, the first 10 min were excluded from analysis. The model requires that the concentration of free DNA substantially exceed that of free YOYO-1, establishing diffusion-limited behavior and a linear relationship between binding-site density and fluorescence intensity [56]. To satisfy this condition, we analyzed fluorescence data collected between 10 and 100 minutes, during which intensity increased linearly (Figure 4e), confirming that available DNA binding sites remained in excess relative to YOYO-1. Although a narrower window (e.g., 20–80 minutes) could impose stricter constraints, lower fluorescence from swollen hydrogels required a broader range to detect measurable intensity changes (Figure 4b).

We approximated DNA concentration using intensity values from late time points (110–120 min), when fluorescence began to saturate:

$$\rho_o(r) \approx \frac{I(r, t_{late})}{\alpha} \quad (3)$$

Radial mapping of DNA density revealed distinct spatial distributions between unswelled and swollen hydrogels. Unswelled hydrogels showed pronounced DNA enrichment at the rim, whereas swollen hydrogels exhibited more uniform DNA distributions (Figure 4c). Two mechanisms may explain this rim-enriched fluorescence observed in unswelled hydrogels: (i) diffusion-limited binding of YOYO-1 and (ii) intrinsic spatial variability in DNA concentration. In the first case, YOYO-1 molecules rapidly bind to DNA near the rim and are locally depleted before diffusing deeper into the hydrogel, producing stronger fluorescence at the edges. This mechanism is unlikely in our system because, by 110–120 min, rim fluorescence had already reached a plateau (Figure S4), indicating that rim binding sites were saturated. If rim depletion were responsible for the rim-enriched signal, continued diffusion after saturation should have increased core fluorescence and reduced the rim–core difference. Instead, the disparity persisted, and if rim-limited binding were dominant, a similar—though weaker—pattern would be expected in swollen hydrogels. However, swollen hydrogels exhibited higher fluorescence intensity in the core than the rim even at early time points, indicating that YOYO-1 was not trapped or depleted near the surface. These observations collectively indicate that the rim–core intensity contrast is not governed by YOYO-1 diffusion-reaction kinetics but instead reflects intrinsic spatial variation in DNA density within the hydrogel network. Therefore, a more plausible explanation is that unswelled μSDs intrinsically possess a higher DNA density near the rim, similar to gradients reported in other polymer networks with nonuniform crosslink densities [57,58]. Swelling then redistributes the DNA network toward a more uniform configuration. This behavior is consistent with diffusion-limited swelling of DNA hairpins [26,37], where hairpins react first near the rim and subsequently penetrate deeper into the network. As the rim-driven expansion progresses, the DNA gradient flattens, yielding the more homogeneous profiles observed in swollen hydrogels (Figure 4c). To further support this explanation, we separately incubated unswelled hydrogels with 5X concentrations of YOYO-1 (5 μM) overnight at room temperature to obtain a radial mapping of DNA density under saturated conditions (Figure S5b). Consistent with the measurements taken in our videos at 110–120 min (Figure 4c), the radial mapping of DNA density in YOYO-1 saturated conditions (Figure S5b) showed a significant enrichment of DNA at the rim. This finding supports our observations of distinct spatial distribution of DNA among unswelled and swollen hydrogels and validates that late time point measurements can effectively capture DNA distribution within our hydrogels.

The observed redistribution of DNA prompted a quantitative analysis of YOYO-1 fluorescence to assess how changes in network structure affect apparent diffusivity. Average fluorescence intensity was significantly higher in unswelled than in swollen ones (Figure 4b), consistent with dilution of DNA content per unit area during swelling [37]. Consequently, diffusivity estimates based on raw (unnormalized) intensity values (Figure S4) reflect DNA density rather than molecular-structure-dependent trends. To quantify diffusivity across μSDs with differing DNA concentration, it is critical to recognize that the diffusion coefficient, D_{eff} , reflects how quickly YOYO-1 molecules penetrate the μSD over time—not how much dye accumulates. Thus, the shape and evolution of the radial intensity profile, rather than its absolute value, encode diffusivity information. Because absolute intensity depends on DNA concentration, comparing raw profiles across samples with different binding capacities would confound diffusion with molecular availability (Figure S4). To address this, all intensity values were normalized to the measured DNA concentration at the rim of each hydrogel ($I(rim, t_{late})$). The rim, being the earliest region exposed to solution, likely reach saturation first and thus provides a consistent reference for maximum YOYO-1 binding. This normalization removes global scaling effects of DNA concentration, enabling shape-based comparisons of diffusion across conditions and reducing noise-related bias. Consequently, diffusivity estimates more faithfully reflect molecular transport rather than differences in binding site density.

Finally, the diffusion constant obtained from our reaction-diffusion model was related to the μSD 's structural properties using the effective diffusion equation:

$$D_{eff} = D_o \Psi \quad (4)$$

D_o is the diffusion coefficient of free YOYO-1 and Ψ as the network coarseness a measurement which reflects the structural properties of our μSD in context of ease of diffusivity. Network coarseness which is referred to as formation factor for porous solid materials [46] is equal to $\Psi = \frac{\varphi}{\tau}$ where φ is the porosity and τ is the tortuosity, which describes the complexity of the diffusion path through the porous network [59]. Under this assumption, network coarseness becomes directly proportional to the measured diffusion coefficient, allowing us to quantify network coarseness without independently resolving porosity and tortuosity. In summary, our fluorescence-based diffusion approach enables a spatially and temporally resolved, data-driven estimation of the concentrations of bound YOYO-1, free YOYO-1, and total DNA within μSDs (Figure 4). These calculations enable an estimation of μSD molecular structure or the network coarseness.

Our results show that average network coarseness increases with μSD swelling, with a statistically significant difference observed between unswelled and swollen μSDs ($p < 0.02$). However, no significant difference was detected between μSDs swollen for 2 hours versus 5 hours, likely due to limitations in our imaging system. Specifically, we had insufficient fluorescence signal at higher swelling levels (Figure

4b) to enable more precise measurements of network coarseness. This technical constraint could be addressed by employing a more powerful laser source, which would be especially important for analyzing network coarseness in μ SDs with lower DNA density such as those subjected to longer swelling periods (>5 hours). Additionally, obtaining a higher sample size may help achieve more statistically significant results, although current protocols make this challenging due to particle movement within the first 9 minutes and the difficulty of maintaining consistent focal plane imaging. Despite this limitation, we observed an average $\sim 25\%$ and $\sim 40\%$ increase in network coarseness after 2 and 5 hours of swelling, highlighting the capability of our workflow to measure the change in molecular-scale permeability of the hydrogel without the need for specialized instruments. Most significantly, our method works with free-floating (membrane-free) μ SDs without any assumptions on geometry of the hydrogel, overcoming the challenges typically posed by the soft and fragile nature of μ SDs [20,38,39]. Controlling molecular permeability and quantifying it without the need for specialized instrumentation will be key to advancing drug delivery and cell culture applications that demand finely tuned material properties.

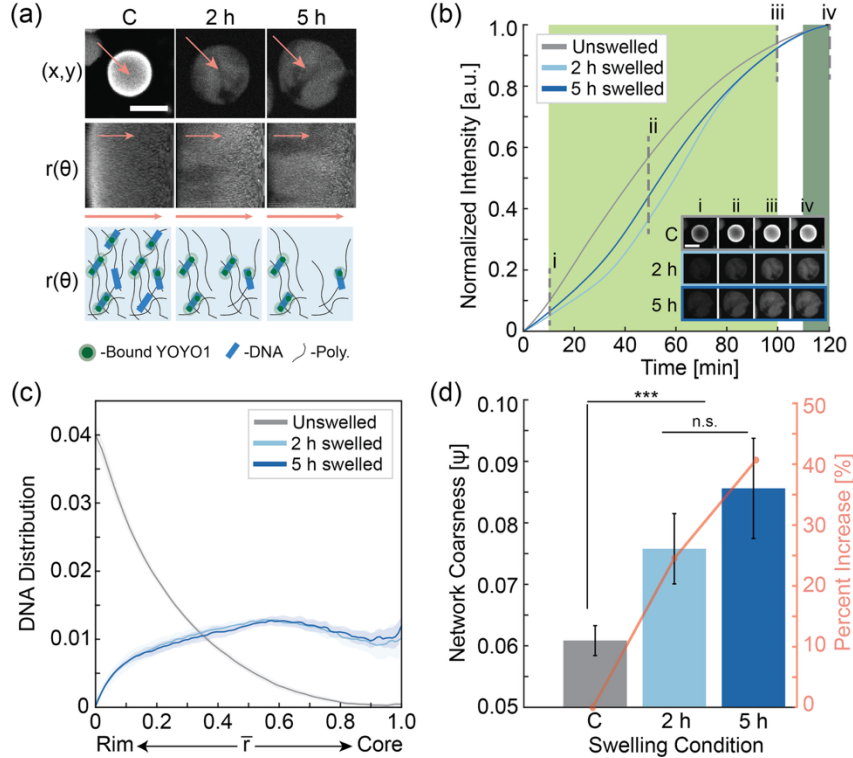


Figure 4: Porosity characterization of DNA-crosslinked hydrogels using a DNA-binding fluorescent probe. (a) Schematic illustration of YOYO-1 diffusion and binding within μ SDs, where the diffusion and reaction rates depend on pore size and the local DNA binding site concentration. (b) Smoothed fluorescence intensity over time. Region I denoting the time window used for reaction-diffusion analysis and transparent region II indicating the plateau phase corresponding to DNA saturation. (c) DNA concentration as a function of radial distance for 110 to 120 min. Shaded regions represent standard error of measurements from $n = 15, 6$, and 11 corresponding to unswelled, 2 h swollen, and 5 h swollen. (d) Material Openness Index (MOI) of μ SDs for each swelling condition with standard deviations. Unswelled and swollen (2 h & 5 h) showed statistical significance with $p < 0.02$ using a two sample t-test. 2 h and 5 h did not show statistical significance.

3.4. Tunable Dissolution Kinetics of μ SDs via a DNA Dissolving Strand

Controlled dissolution of μ SDs is essential for applications that require retrieval of encapsulated cells after an assay. To enable this capability, a dissolving strand was designed to be fully complementary to S1-C, such that μ SDs may be dissolved with the same universal strand regardless of their swollen status. The dissolving strand binds to a three-nucleotide length single-stranded region on S1-C in the S1-C:S1-C' duplex of the μ SD, displacing S1-C' and thereby disrupting the gel matrix. We validated the dissolving efficacy using polyacrylamide gel electrophoresis (PAGE) (Figure S7) and evaluated whether a complementary DNA dissolving strand could modulate the dissolution kinetics of μ SDs in a programmable manner.

Unswelled μ SDs were incubated with dissolving strand concentrations of 0, 0.5, 1, 2, and 4 μ M to evaluate whether dissolution rate could be modulated through strand concentration. Time-lapse imaging (Figure 5a, Figure S8a,b) and normalized μ SD counts (fraction remaining relative to t_0 , Figure 5b) revealed strong concentration dependency: 0 μ M samples remained stable, 2-4 μ M conditions dissolved rapidly, and intermediate concentration (0.5-1 μ M) showed slower, multi-phase decreases. These results confirm that μ SD dissolution kinetics are tunable by adjusting dissolving strand concentration. We further confirmed that hydrogel dissolution is sequence-specific by incubating μ SD with scrambled DNA sequences, which showed that the hydrogels do not dissolve in the presence of non-complementary DNA (Figure S9).

To relate dissolution to structural changes, we extended our analysis of network coarseness, ψ . ψ determined based on diffusion kinetics (Section 3.3), displayed an inverse relationship with DNA concentration measured with YOYO-1 Intensity in the previous section ($R^2 = 0.86$, Figure S8c). We applied this relationship to dissolution by approximating network openness, ψ_{poly} , using polymer concentration, C_{poly} :

$$\psi_{poly} \propto \frac{1}{C_{poly}} \approx \frac{1}{k_b (I_{poly})} \quad (5)$$

Here, ψ_{poly} is inferred from fluorescence intensity, I_{poly} , used as a proxy for polymer concentration, C_{poly} . A calibration factor k_b relates intensity to polymer concentration [52]. This inverse dependence aligns with free volume theory ($f = \frac{C_{FS}}{C_{poly}}$) [60], in which decreasing polymer concentration increases network openness. Thus, as μ SDs dissolve and polymer content decreases, ψ_{poly} increases. This principle has been widely used to describe diffusivity in polymeric systems [61,62] and is consistent with the ψ -DNA-density relationship observed in Section 3.3 (Figure S8c).

As μ SDs dissolved, they exhibited lower signal-to-noise ratios at later time points and became difficult to segment when clumped particularly near well walls. Because of this, not all particles could be tracked for the full duration of the experiment. To account for these limitations, we leveraged the observation that across all conditions, maximum fluorescent intensity decreased approximately linearly over time (Figure S8e,f). We quantified dissolution using the slope of fluorescence intensity over time, which can be estimated reliably from only a few frames. Averaging slopes across particles thus provides a robust estimate of the rate of network coarsening even when individual trajectories are incomplete. The slope magnitude ($\frac{dI_{poly}}{dt}$) reflects the rate of polymer loss ($\frac{dC_{poly}}{dt}$) and thereby the rate of network-coarseness increases through Equation (5). The slope therefore serves as a dissolution rate constant quantifying the kinetics of μ SDs degradation.

The average dissolution behavior of the μ SD for each experimental condition was determined from the mean slope across all samples. The standard error of the fitted slope was calculated as $SE = \sqrt{\frac{\sigma^2}{\sum(x_i - x_{avg})^2}}$ [63–66] of slope derived from Figure S8 where $\sigma^2 = \frac{1}{n-1} \sum r_i$ is the residual variance of the linear regression of our data where r_i is the residual. $\sum(x_i - x_{avg})^2$ is the sum of squared deviations of the independent variable from its mean. These calculations enable visualization of the dissolution behavior of all hydrogels under each experimental condition along with estimated standard error of our model.

Another key observation was the intermittent appearance of a diffuse fluorescent halo surrounding the μ SDs following addition of the dissolving strand, leading to an apparent increase in the measured diameter for a subset of hydrogels (Figure S8d). This cloud presumably originates from dissolved polyacrylamide that does not immediately diffuse away, depending on local diffusion kinetics (proximity to channel wall). Because this cloud overlapped with the hydrogel boundary, our detection algorithms could not consistently distinguish intact μ SDs from surrounding polymer residue, making diameter measurements unreliable and prone to artificial increase or decrease (Figure S8d). To address this, we quantified the maximum fluorescence intensity within each μ SD (Figure S8f) rather than average intensity (Figure S8e), providing a more reliable metric for remaining polymer content. This approach helped mitigate potential confounding effects from polymer residue surrounding the μ SDs, providing a more reliable measurement of the remaining polyacrylamide content in the hydrogels. Although maximum intensity measurements are, in principle, more sensitive to isolated high-intensity defects, manual inspection did not reveal any obvious artifacts, and the temporal trends in maximum intensity (Figure S8e) were consistent with those obtained using average intensity (Figure S8f). Together, these models and analytical assumptions enable accurate quantification of the molecular changes underlying network coarsening observed in our data.

Consistent with particle-counting data (Figure 5b), network coarseness increased more rapidly at higher dissolving strand concentration (Figure 5c), while the 0 μ M condition remained at baseline. Interestingly, each concentration exhibited two subpopulations of fast- and slow-dissolving μ SDs. Further inspection revealed that dissolution rate depends on the μ SD's radial position within the well (Figure S6, Supplementary Video). μ SDs nearer the well center dissolved faster than those near the walls (Figure S10). This positional dependence arises from transport limitations inherent to static well conditions, which are also characteristic of many commonly used static or confined assays [24,25]. In such environments, fluid near the walls forms a stagnant diffusion boundary layer that reduces solute transport [67–70]. Near-wall hydrodynamic effects, where proximity to a solid boundary reduces effective diffusivity (Faxén's law [69,70]), further slow the delivery of dissolving strands to μ SDs near the wall. Despite bimodal dissolution behavior, the dissolution constant-defined as the absolute slope $\left| \frac{dI_{poly}}{dt} \right|$ showed a clear concentration-dependent increase (Figure 5d). The nonlinear dependence of the dissolution constant on strand concentration suggests that both delivery kinetics of the dissolving strand and the strand-network reaction mechanism may contribute to the overall dissolution rate, highlighting the need for further mechanistic studies to disentangle these coupled processes.

These results demonstrate that μ SD dissolution can be precisely tuned through the concentration of dissolving DNA strand while also highlighting how static fluid environments impose transport limitations that influence observed dissolution kinetics. These insights are important for workflows that rely on controlled μ SD dissolution, such as retrieval of encapsulated cells after functional assays.

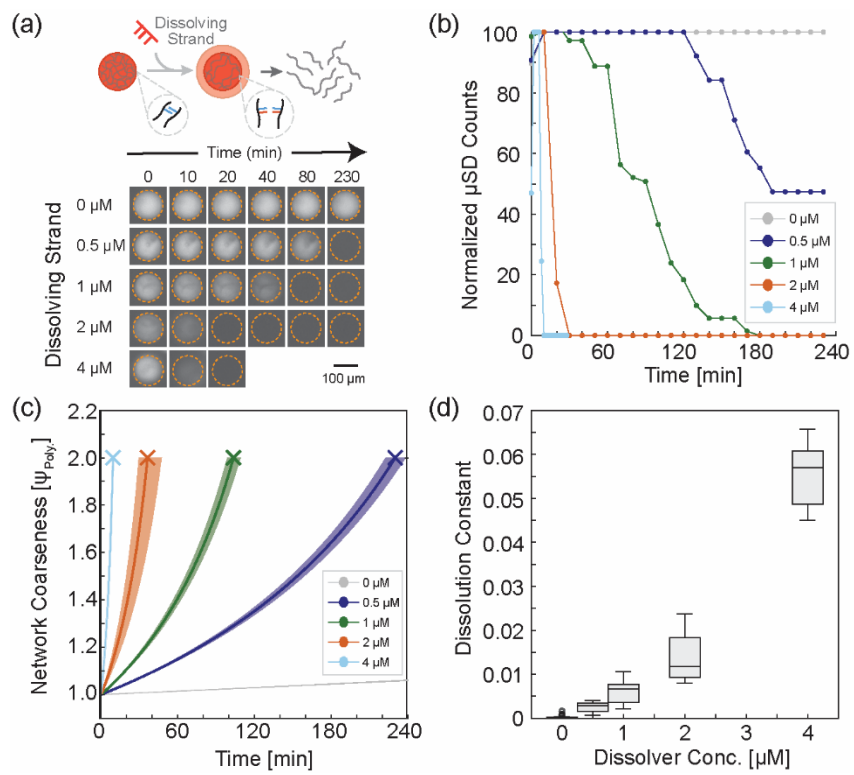


Figure 5: Modular Control of Dissolving μ SD (a) Schematic showing the dissolution process of μ SDs. Dissolved polymer initially forms a cloud-like residue around the hydrogel before diffusing into the solution. Representative images show individual hydrogels dissolving. (b) μ SD counts (normalized to the second frame) decrease over time, showing the progressive dissolution of hydrogels. Values were normalized to the second frame because the μ SDs typically had not fully settled in the first acquired frame. (c) Network coarseness calculated using polymer concentration plotted against time for varying dissolving strand concentrations. Solid lines represent average fitting. The 'x' markers denote the estimated final analyzable timepoints before μ SDs dissolved below detection. Shaded represent standard error of calculated network coarseness. (d) Dissolution constant as a function of dissolver concentration.

4. Conclusion

μ SDs hold tremendous potential for biomedical applications, yet their widespread use has been limited by the need for robust microscale fabrication methods suitable for single cell encapsulation and related applications. In this work, we developed a droplet microfluidic system capable of encapsulating cells and demonstrated its biocompatibility by maintaining high cell viability. To further maximize utility, we designed a material-efficient workflow, ensuring that even small volumes of valuable DNA solutions could be efficiently used for hydrogel fabrication.

We demonstrated the ability to regulate isotropic swelling of μ SDs and showed that this swelling is directly associated with changes in molecular network properties—an important factor for systems where diffusion must be precisely controlled. We also established an accessible workflow to quantify these molecular-level changes without the need for specialized equipment. This method provides a versatile foundation that in the future can be extended to μ SDs of any shape or to capture spatial variations in network openness within individual hydrogels as technical limitations in fluorophore intensity, laser strength, and microscope resolution are overcome. Finally, we demonstrate that the dissolution kinetics of DNA-based hydrogels can be effectively modulated by varying the concentration of dissolving strands. The dissolution process is influenced by both reaction kinetics and transport mechanics, offering valuable insights for designing hydrogels for controlled drug release and cell delivery applications. Our fabrication and characterization workflow could be used for future applications with more complex DNA designs and kinetic control, broadening the scope of the platform. Collectively, these advances establish a robust, biocompatible, and efficient system for fabricating, controlling, and characterizing μ SDs, with wide-ranging potential in drug delivery, biosensing, single-cell encapsulation, and other applications that require precise regulation of molecular permeability and swelling kinetics.

5. Acknowledgements

This work is supported by the Elsa U. Pardee foundation and NIH IMAT (R21CA251027). The authors thank Dr. Atsushi Miyawaki (RIKEN Institute, Japan) for generously providing the plasmids used to modify the cells in this study. Some portions of the code used in this study were generated with the assistance of ChatGPT (OpenAI), which also aided in restructuring sections of the manuscript for improved clarity and readability. All analyses and interpretations were performed and verified by the authors.

References

- Wu R, Li W, Yang P, Shen N, Yang A, Liu X, et al. DNA hydrogels and their derivatives in biomedical engineering applications. *J Nanobiotechnology*. 2024;22:518. <https://doi.org/10.1186/s12951-024-02791-z>
- Hu Y, Gao S, Lu H, Ying JY. Acid-Resistant and Physiological pH-Responsive DNA Hydrogel Composed of A-Motif and i-Motif toward Oral Insulin Delivery. *J Am Chem Soc*. 2022;144:5461–70. <https://doi.org/10.1021/jacs.1c13426>

3. Song J, Im K, Hwang S, Hur J, Nam J, Ahn G-O, et al. DNA hydrogel delivery vehicle for light-triggered and synergistic cancer therapy. *Nanoscale*. 2015;7:9433–7. <https://doi.org/10.1039/C5NR00858A>

4. Pan G, Mou Q, Ma Y, Ding F, Zhang J, Guo Y, et al. pH-Responsive and Gemcitabine-Containing DNA Nanogel To Facilitate the Chemodrug Delivery. *ACS Appl Mater Interfaces*. 2019;11:41082–90. <https://doi.org/10.1021/acsami.9b14892>

5. Chen Z, Zhang H, Huang J, Weng W, Geng Z, Li M, et al. DNA-encoded dynamic hydrogels for 3D bioprinted cartilage organoids. *Mater Today Bio*. 2025;31:101509. <https://doi.org/10.1016/j.mtbio.2025.101509>

6. Song P, Ye D, Zuo X, Li J, Wang J, Liu H, et al. DNA Hydrogel with Aptamer-Toehold-Based Recognition, Cloaking, and Decloaking of Circulating Tumor Cells for Live Cell Analysis. *Nano Lett*. 2017;17:5193–8. <https://doi.org/10.1021/acs.nanolett.7b01006>

7. Rubanov M, Cole J, Lee H-J, Soto Cordova LG, Chen Z, Gonzalez E, et al. Multi-domain automated patterning of DNA-functionalized hydrogels. Dubey N, editor. *PLOS ONE*. 2024;19:e0295923. <https://doi.org/10.1371/journal.pone.0295923>

8. Fern J, Shi R, Liu Y, Xiong Y, Gracias DH, Schulman R. Swelling characteristics of DNA polymerization gels. *Soft Matter*. 2023;19:6525–34. <https://doi.org/10.1039/D3SM00321C>

9. Henkel M, Kimna C, Lieleg O. DNA Crosslinked Mucin Hydrogels Allow for On-Demand Gel Disintegration and Triggered Particle Release. *Macromol Biosci*. 2024;24:2300427. <https://doi.org/10.1002/mabi.202300427>

10. Huang F, Chen M, Zhou Z, Duan R, Xia F, Willner I. Spatiotemporal patterning of photoresponsive DNA-based hydrogels to tune local cell responses. *Nat Commun*. 2021;12:2364. <https://doi.org/10.1038/s41467-021-22645-8>

11. Liao W-C, Lilienthal S, Kahn JS, Riutin M, Sohn YS, Nechushtai R, et al. pH- and ligand-induced release of loads from DNA–acrylamide hydrogel microcapsules. *Chem Sci*. 2017;8:3362–73. <https://doi.org/10.1039/C6SC04770J>

12. Guo W, Qi X-J, Orbach R, Lu C-H, Freage L, Mironi-Harpaz I, et al. Reversible Ag+-crosslinked DNA hydrogels. *Chem Commun*. 2014;50:4065. <https://doi.org/10.1039/c3cc49140d>

13. Ma Y, Mao Y, An Y, Tian T, Zhang H, Yan J, et al. Target-responsive DNA hydrogel for non-enzymatic and visual detection of glucose. *The Analyst*. 2018;143:1679–84. <https://doi.org/10.1039/C8AN00010G>

14. Zheng M, Liu H, Ye J, Ni B, Xie Y, Wang S. Target-responsive aptamer-cross-linked hydrogel sensors for the visual quantitative detection of aflatoxin B1 using exonuclease I-Triggered target cyclic amplification. *Food Chem X*. 2022;15:100395. <https://doi.org/10.1016/j.fochx.2022.100395>

15. Wang X, He L, Rong X, Liu L, Yin Y, Zhao X, et al. DNA aptamer-crosslinked hydrogel sensor: Design, mechanism and application for food safety analysis. *Trends Food Sci Technol*. 2025;156:104846. <https://doi.org/10.1016/j.tifs.2024.104846>

16. Gu Y, Distler ME, Cheng HF, Huang C, Mirkin CA. A General DNA-Gated Hydrogel Strategy for Selective Transport of Chemical and Biological Cargos. *J Am Chem Soc*. 2021;143:17200–8. <https://doi.org/10.1021/jacs.1c08114>

17. Yao C, Tang H, Wu W, Tang J, Guo W, Luo D, et al. Double Rolling Circle Amplification Generates Physically Cross-Linked DNA Network for Stem Cell Fishing. *J Am Chem Soc*. 2020;142:3422–9. <https://doi.org/10.1021/jacs.9b11001>

18. Wei Y, Wang K, Luo S, Li F, Zuo X, Fan C, et al. Programmable DNA Hydrogels as Artificial Extracellular Matrix. *Small*. 2022;18:2107640. <https://doi.org/10.1002/smll.202107640>

19. Jin J, Xing Y, Xi Y, Liu X, Zhou T, Ma X, et al. A Triggered DNA Hydrogel Cover to Envelop and Release Single Cells. *Adv Mater*. 2013;25:4714–7. <https://doi.org/10.1002/adma.201301175>

20. Li Y, Ma Y, Jiao X, Li T, Lv Z, Yang CJ, et al. Control of capillary behavior through target-responsive hydrogel permeability alteration for sensitive visual quantitative detection. *Nat Commun*. 2019;10:1036. <https://doi.org/10.1038/s41467-019-08952-1>

21. Li J, Song W, Li F. Polymeric DNA Hydrogels and Their Applications in Drug Delivery for Cancer Therapy. *Gels*. 2023;9:239. <https://doi.org/10.3390/gels9030239>

22. Wang D, Hu Y, Liu P, Luo D. Bioreponsive DNA Hydrogels: Beyond the Conventional Stimuli Responsiveness. *Acc Chem Res*. 2017;50:733–9. <https://doi.org/10.1021/acs.accounts.6b00581>

23. Lyu D, Chen S, Guo W. Liposome Crosslinked Polyacrylamide/DNA Hydrogel: a Smart Controlled-Release System for Small Molecular Payloads. *Small*. 2018;14:1704039. <https://doi.org/10.1002/smll.201704039>

24. Zhang J, Guo Y, Pan G, Wang P, Li Y, Zhu X, et al. Injectable Drug-Conjugated DNA Hydrogel for Local Chemotherapy to Prevent Tumor Recurrence. *ACS Appl Mater Interfaces*. 2020;12:21441–9. <https://doi.org/10.1021/acsami.0c03360>

25. Singh S, Mishra A, Kumari R, Sinha KK, Singh MK, Das P. Carbon dots assisted formation of DNA hydrogel for sustained release of drug. *Carbon*. 2017;114:169–76. <https://doi.org/10.1016/j.carbon.2016.12.020>

26. Fern J, Schulman R. Modular DNA strand-displacement controllers for directing material expansion. *Nat Commun*. 2018;9:3766. <https://doi.org/10.1038/s41467-018-06218-w>

27. Mo F, Jiang K, Zhao D, Wang Y, Song J, Tan W. DNA hydrogel-based gene editing and drug delivery systems. *Adv Drug Deliv Rev*. 2021;168:79–98. <https://doi.org/10.1016/j.addr.2020.07.018>

28. Zhu H, Wu J, Zhao J, Yu L, Liyariita BR, Xu X, et al. Dual-functional DNA nanogels for anticancer drug delivery. *Acta Biomater*. 2024;175:240–9. <https://doi.org/10.1016/j.actbio.2023.12.013>

29. Li Y, Huang D, Zhang Y, Xiao Y, Zhang X. Microfluidic-assisted engineering of hydrogels with microscale complexity. *Acta Biomater*. 2025;199:1–17. <https://doi.org/10.1016/j.actbio.2025.05.023>

30. Ward K, Fan ZH. Mixing in microfluidic devices and enhancement methods. *J Micromechanics Microengineering*. 2015;25:094001. <https://doi.org/10.1088/0960-1317/25/9/094001>

31. Leman M, Abouakil F, Griffiths AD, Tabeling P. Droplet-based microfluidics at the femtolitre scale. *Lab Chip*. 2015;15:753–65. <https://doi.org/10.1039/C4LC01122H>

32. Li F, Lyu D, Liu S, Guo W. DNA Hydrogels and Micogels for Biosensing and Biomedical Applications. *Adv Mater*. 2020;32:1806538. <https://doi.org/10.1002/adma.201806538>

33. Nishikawa J, Tamura Y, Fujii T, Fukuda S, Yoneda S, Yamaura N, et al. Far-Ultraviolet Light at 222 nm Affects Membrane Integrity in Monolayered DLD1 Colon Cancer Cells. *Int J Mol Sci*. 2024;25:7051. <https://doi.org/10.3390/ijms25137051>

34. Xu F, Dawson C, Lamb M, Mueller E, Stefanek E, Akbari M, et al. Hydrogels for Tissue Engineering: Addressing Key Design Needs Toward Clinical Translation. *Front Bioeng Biotechnol*. 2022;10:849831. <https://doi.org/10.3389/fbioe.2022.849831>

35. Okumura S, Hapsianto BN, Lobato-Dauzier N, Ohno Y, Benner S, Torii Y, et al. Morphological Manipulation of DNA Gel Microbeads with Biomolecular Stimuli. *Nanomaterials*. 2021;11:293. <https://doi.org/10.3390/nano11020293>

36. Kim T, Park S, Lee M, Baek S, Lee JB, Park N. DNA hydrogel microspheres and their potential applications for protein delivery and live cell monitoring. *Biomicrofluidics*. 2016;10:034112. <https://doi.org/10.1063/1.4953046>

37. Zimmerman BK, Schulman R, Nguyen TD. Growth-induced Donnan exclusion influences swelling kinetics in highly charged dynamic polymerization hydrogels. *Extreme Mech Lett*. 2025;78:102354. <https://doi.org/10.1016/j.eml.2025.102354>

38. Li S, Nih LR, Bachman H, Fei P, Li Y, Nam E, et al. Hydrogels with precisely controlled integrin activation dictate vascular patterning and permeability. *Nat Mater*. 2017;16:953–61. <https://doi.org/10.1038/nmat4954>

39. Tokarev I, Orlov M, Minko S. Responsive Polyelectrolyte Gel Membranes. *Adv Mater*. 2006;18:2458–60. <https://doi.org/10.1002/adma.200601288>

40. Jayawardena I, Turunen P, Girms BC, Rowan A, Corrie S, Grøndahl L. Evaluation of techniques used for visualisation of hydrogel morphology and determination of pore size distributions. *Mater Adv*. 2023;4:669–82. <https://doi.org/10.1039/D2MA00932C>

41. Tolentino MAK, Du EY, Silvani G, Pandzic E, Kilian KA, Gooding JJ. Decoding Hydrogel Porosity: Advancing the Structural Analysis of Hydrogels for Biomedical Applications. *Adv Healthc Mater*. 2025;14:2500658. <https://doi.org/10.1002/adhm.202500658>

42. Li S, Chen L. DNA hydrogels for biomedical applications: Advances and prospects. *Chem Eng J*. 2025;508:161157. <https://doi.org/10.1016/j.cej.2025.161157>

43. Ma D, Marshall JS, Wu J. Measurement of ultrasound-enhanced diffusion coefficient of nanoparticles in an agarose hydrogel. *J Acoust Soc Am*. 2018;144:3496–502. <https://doi.org/10.1121/1.5083828>

44. Rashapov R, Imami F, Gostick JT. A method for measuring in-plane effective diffusivity in thin porous media. *Int J Heat Mass Transf*. 2015;85:367–74. <https://doi.org/10.1016/j.ijheatmasstransfer.2015.01.101>

45. Brown LF, Travis BJ. Using diffusion measurements to determine pore-size distributions in porous materials. *Chem Eng Sci*. 1983;38:843–7. [https://doi.org/10.1016/0009-2509\(83\)80004-9](https://doi.org/10.1016/0009-2509(83)80004-9)

46. Benning JL, Barnes DL. Comparison of modeling methods for the determination of effective porosities and diffusion coefficients in through-diffusion tests. *Water Resour Res*. 2009;45:2008WR007236. <https://doi.org/10.1029/2008WR007236>

47. Serag MF, Abadi M, Habuchi S. Single-molecule diffusion and conformational dynamics by spatial integration of temporal fluctuations. *Nat Commun*. 2014;5:5123. <https://doi.org/10.1038/ncomms6123>

48. Sinha N, Subedi N, Wimmers F, Soennichsen M, Tel J. A Pipette-Tip Based Method for Seeding Cells to Droplet Microfluidic Platforms. *J Vis Exp*. 2019;57848. <https://doi.org/10.3791/57848>

49. Zhang L, Chen K, Zhang H, Pang B, Choi C, Mao AS, et al. Microfluidic Templated Multicompartment Microgels for 3D Encapsulation and Pairing of Single Cells. *Small*. 2018;14:1702955. <https://doi.org/10.1002/smll.201702955>

50. Sakaue-Sawano A, Kobayashi T, Ohtawa K, Miyawaki A. Drug-induced cell cycle modulation leading to cell-cycle arrest, nuclear mis-segregation, or endoreplication. *BMC Cell Biol*. 2011;12:2. <https://doi.org/10.1186/1471-2121-12-2>

51. Zadeh JN, Steenberg CD, Bois JS, Wolfe BR, Pierce MB, Khan AR, et al. NUPACK: Analysis and design of nucleic acid systems. *J Comput Chem*. 2011;32:170–3. <https://doi.org/10.1002/jcc.21596>

52. Su Z, Zhang Y, Liu W, Han R, Zhao X, Shi X, et al. A Quantitative Approach to Determine Hydrophobe Content of Associating Polyacrylamide Using a Fluorescent Probe. *Mol Basel Switz*. 2023;28:4152. <https://doi.org/10.3390/molecules28104152>

53. Pal A, Gope A, Sengupta A. Drying of bio-colloidal sessile droplets: Advances, applications, and perspectives. *Adv Colloid Interface Sci*. 2023;314:102870. <https://doi.org/10.1016/j.cis.2023.102870>

54. Rye HS, Yue S, Wemmer DE, Quesada MA, Haugland RP, Mathies RA, et al. Stable fluorescent complexes of double-stranded DNA with bis-intercalating asymmetric cyanine dyes: properties and applications. *Nucleic Acids Res*. 1992;20:2803–12. <https://doi.org/10.1093/nar/20.11.2803>

55. Stastna M, Steinmoeller D. Modeling active tracers. *Phys Ecol Fluids* [Internet]. Elsevier; 2023 [cited 2025 Sept 30]. p. 31–50. <https://doi.org/10.1016/B978-0-32-391244-0.00013-9>

56. Zhang Y, Kuang X, Yi J, Sun T, Guo Q, Gu H, et al. Revolutionizing the capture efficiency of ultrasensitive digital ELISA *via* an antibody oriented-immobilization strategy. *J Mater Chem B*. 2024;12:10041–53. <https://doi.org/10.1039/D4TB01141D>

57. Seiffert S. Origin of nanostructural inhomogeneity in polymer-network gels. *Polym Chem*. 2017;8:4472–87. <https://doi.org/10.1039/C7PY01035D>

58. Hao P-T, Li S-S, Xue C-D, Qin K-R. Spatial heterogeneity in Hydrogels: Nanoparticle Diffusivity as a probe for network dynamics. *Microchem J*. 2025;214:114092. <https://doi.org/10.1016/j.microc.2025.114092>

59. Pismen LM. Diffusion in porous media of a random structure. *Chem Eng Sci*. 1974;29:1227–36. [https://doi.org/10.1016/0009-2509\(74\)80122-3](https://doi.org/10.1016/0009-2509(74)80122-3)

60. Zhou C, Huang Y, Zheng Y, Hua Z. Hydrogen permeation behavior of rubber sealing materials for hydrogen infrastructure: Recent advances and perspectives. *Int J Hydrog Energy*. 2024;59:742–54. <https://doi.org/10.1016/j.ijhydene.2024.02.042>

61. Tsai Y-C, Chiu C-C. Solute Diffusivity and Local Free Volume in Cross-Linked Polymer Network: Implication of Optimizing the Conductivity of Polymer Electrolyte. *Polymers*. 2022;14:2061. <https://doi.org/10.3390/polym14102061>

62. Rah K. Rescaled Free-Volume Theory of Diffusivity of Polystyrene in Various Organic Solvents. *ACS Omega*. 2025;10:1303–7. <https://doi.org/10.1021/acsomega.4c08891>

63. Wheelan CJ. Naked statistics: stripping the dread from the data. First published as a Norton paperback. New York London: W.W. Norton & Company; 2014.

64. Zwillinger D. Standard mathematical tables and formulae. 31st ed. Boca Raton London New York [etc.]: Chapman & Hall/CRC; 2003.

65. Kotz S, editor. Encyclopedia of statistical sciences. New York, NY: Wiley; 1982.

66. Everitt B, Skrondal A. The Cambridge dictionary of statistics. 4th edition. Cambridge New York: Cambridge University Press; 2010.

67. Banerjee A, Kihm KD. Experimental verification of near-wall hindered diffusion for the Brownian motion of nanoparticles using evanescent wave microscopy. *Phys Rev E*. 2005;72:042101. <https://doi.org/10.1103/PhysRevE.72.042101>

68. Agosta L, Briels W, Hermansson K, Dzugutov M. The entropic origin of the enhancement of liquid diffusion close to a neutral confining surface. *J Chem Phys.* 2024;161:091102. <https://doi.org/10.1063/5.0224016>

69. Chio CC, Tse Y-LS. Hindered Diffusion near Fluid–Solid Interfaces: Comparison of Molecular Dynamics to Continuum Hydrodynamics. *Langmuir.* 2020;36:9412–23. <https://doi.org/10.1021/acs.langmuir.0c01228>

70. Sharma P, Ghosh S, Bhattacharya S. A high-precision study of hindered diffusion near a wall. *Appl Phys Lett.* 2010;97:104101. <https://doi.org/10.1063/1.3486123>

Supplementary Materials

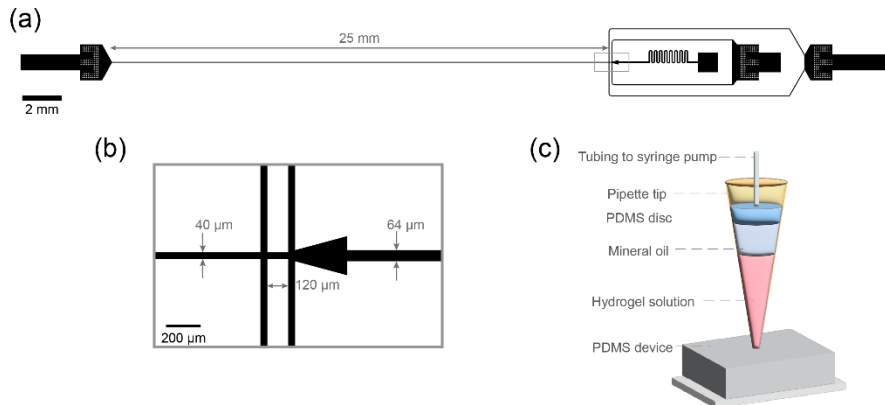


Figure S1: (a) Geometry of 3-inlet microfluidic droplet generator. Details and dimensions of droplet generation region is shown in (b). (c) Schematic of the pipette tip used to inject the hydrogel into the microfluidic device.

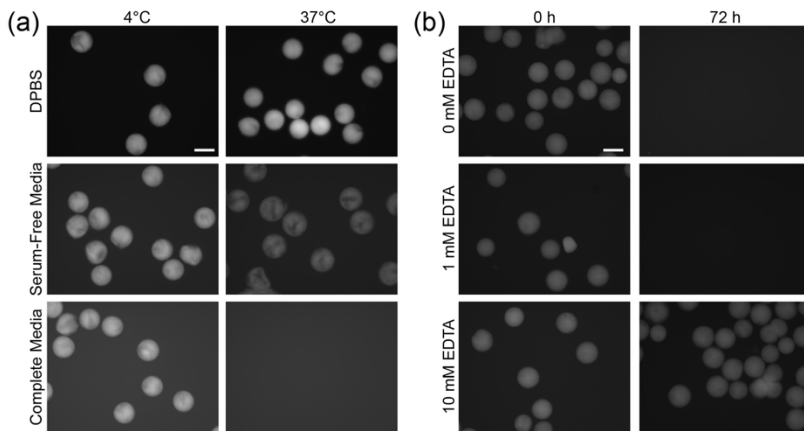


Figure S2: (a) Representative images of μ SDs in DPBS with Ca^{2+} and Mg^{2+} , serum free media (IMDM), and complete media (IMDM + 10% FBS + 1% Penicillin-streptomycin) after 48 h. At 4°C, the μ SDs in serum-free media and complete media maintained their size ($d = 11.2 \pm 3.5$ ($n=10$) and 109.4 ± 2.5 ($n=8$), respectively) as compared to the initial population (113.1 ± 3.8 μ m). At 37°C, however, the μ SDs increased in diameter to 126.6 ± 4.7 μ m ($n=9$) in serum free media and completely degraded in complete media, likely due to increased DNase activity at higher temperatures. (b) The μ SDs were incubated for 72 h in complete media with EDTA, which inhibits DNase activity. 10 mM of EDTA was sufficient to inhibit DNase degradation of the μ SD, demonstrating that the hydrogel degradation in complete media is due to DNase activity. Scale bars are 100 μ m.

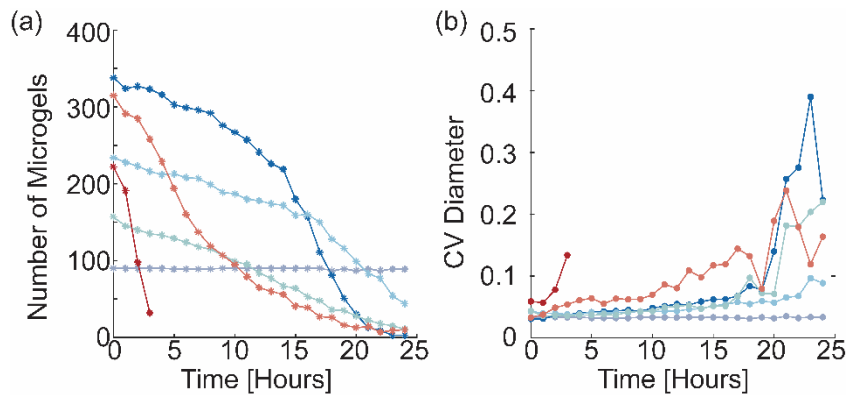


Figure S3: (a) Count of μ SD (b) Coefficient of Variation (CV) of diameter as function of time for swelling data in section 3.4.

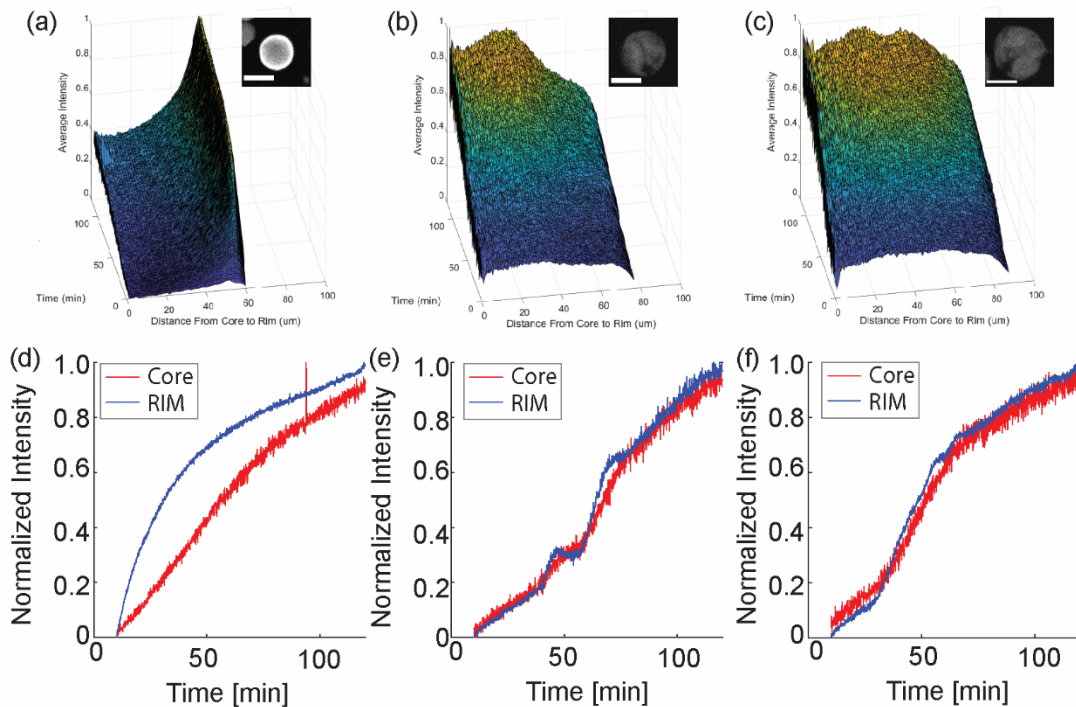


Figure S4: Representative intensity data as a function of time and distance from core for (a) unswelled, (b) 2 hr swollen, and (c) 5 hr swollen. The average intensity of particle as a function of time at core and RIM of μ SD. No smoothing is applied to this data to illustrate artifacts and noise a present in raw data which are removed by the smoothdata() function in MATLAB.

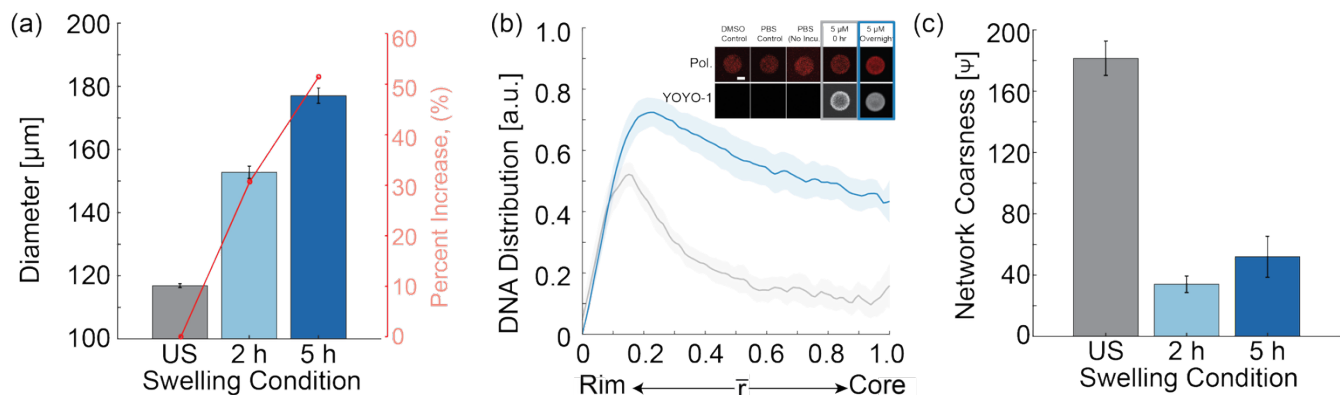


Figure S5: (a) Diameter of particles in YOYO-1 diffusion experiments. (b) DNA Distribution (Intensity) of unswelled hydrogels as a function of normalized distance from rim for 5 μ M YOYO-1 incubated for 0 hour (n=11) and overnight (n=8). Inset images of unswelled hydrogels with DMSO, PBS, and 5 μ M YOYO-1 incubated overnight at room temperature. In addition, images with PBS just prior to and <10 min after addition of 5 μ M YOYO-1. Contrast was adjusted per image to emphasize rim to core intensity difference. (c) Network Coarseness calculated without normalization of data

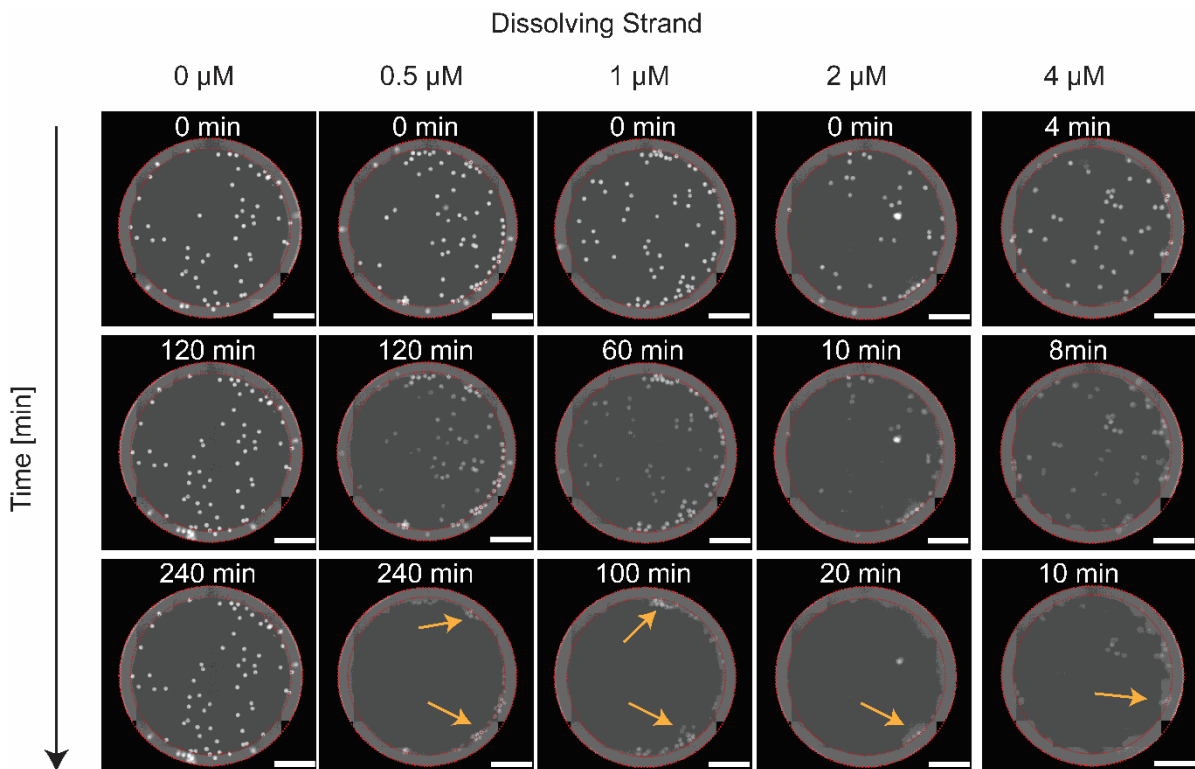


Figure S6: Whole well snap shots of dissolving μ SD. Whole well images are converted to an 8-bit from 16-bit. Red dotted lines are added for well wall boundaries. Scale bars: 1000 μ m.

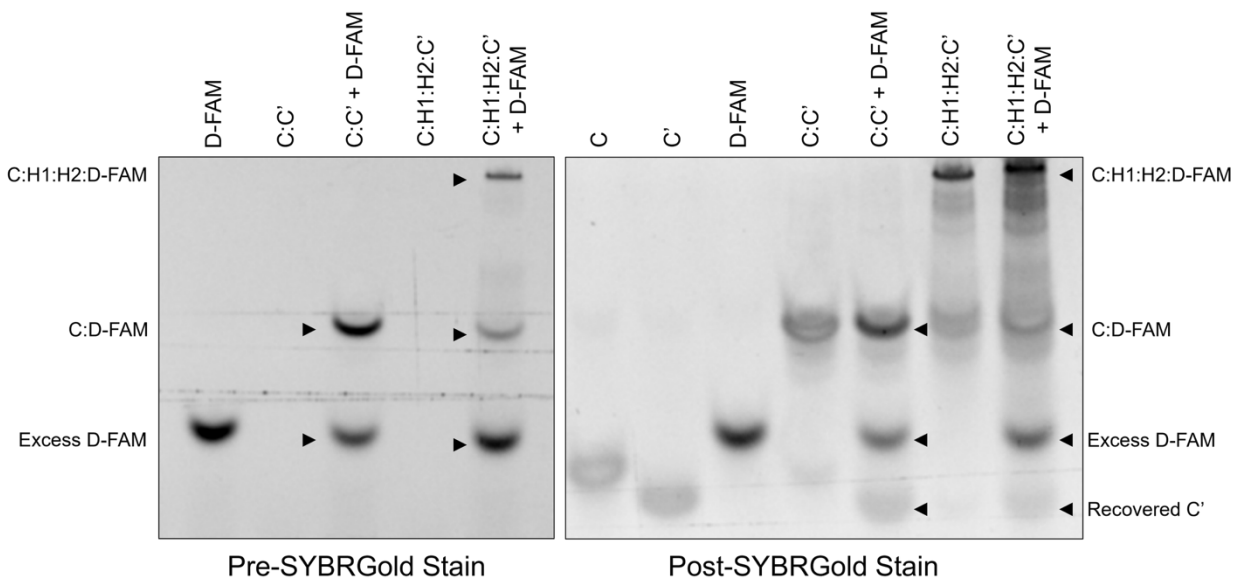


Figure S7: In order to confirm that C' is displaced in both unswelled and swollen hydrogel particles, we conducted PAGE using C and C' strands lacking the Acrydite™ modification. We tagged D with FAM (D-FAM) to aid in distinguishing bands of similarly sized strands. The single stranded components used as controls are C, C', and D-FAM prepared in 1x DPBS. We also prepared complexes in 1x DPBS that resemble unswelled and swollen hydrogels: C:C' (unswelled) and C:H1:H2:C' (swollen), where colons denote hybridized complexes. To minimize bands on the gel in the hybridization chain reaction condition (swollen), we prepared complexes with equal amounts of DNA totaling 100 μ g in 25 μ L for single stranded components and 50 μ g in 75 μ L for the complexes. All samples are incubated at room temperature for 2 hours, at which point twice as much D-FAM (100 μ g) is added to an aliquot each of C:C' and C:H1:H2:C'. Samples are then incubated at room temperature for 30 minutes protected from light. All samples are diluted 1:200 and run on 15% non-denaturing PAGE at 120V. The gel is first visualized without staining to mark where D-FAM appears (left). It is then stained with SYBRGold to visualize the remaining components (right). In the lanes where D-FAM is added to the unswelled and swollen complexes, C' is recovered, indicating that the dissolver has successfully displaced C', thus separating it from the complex.

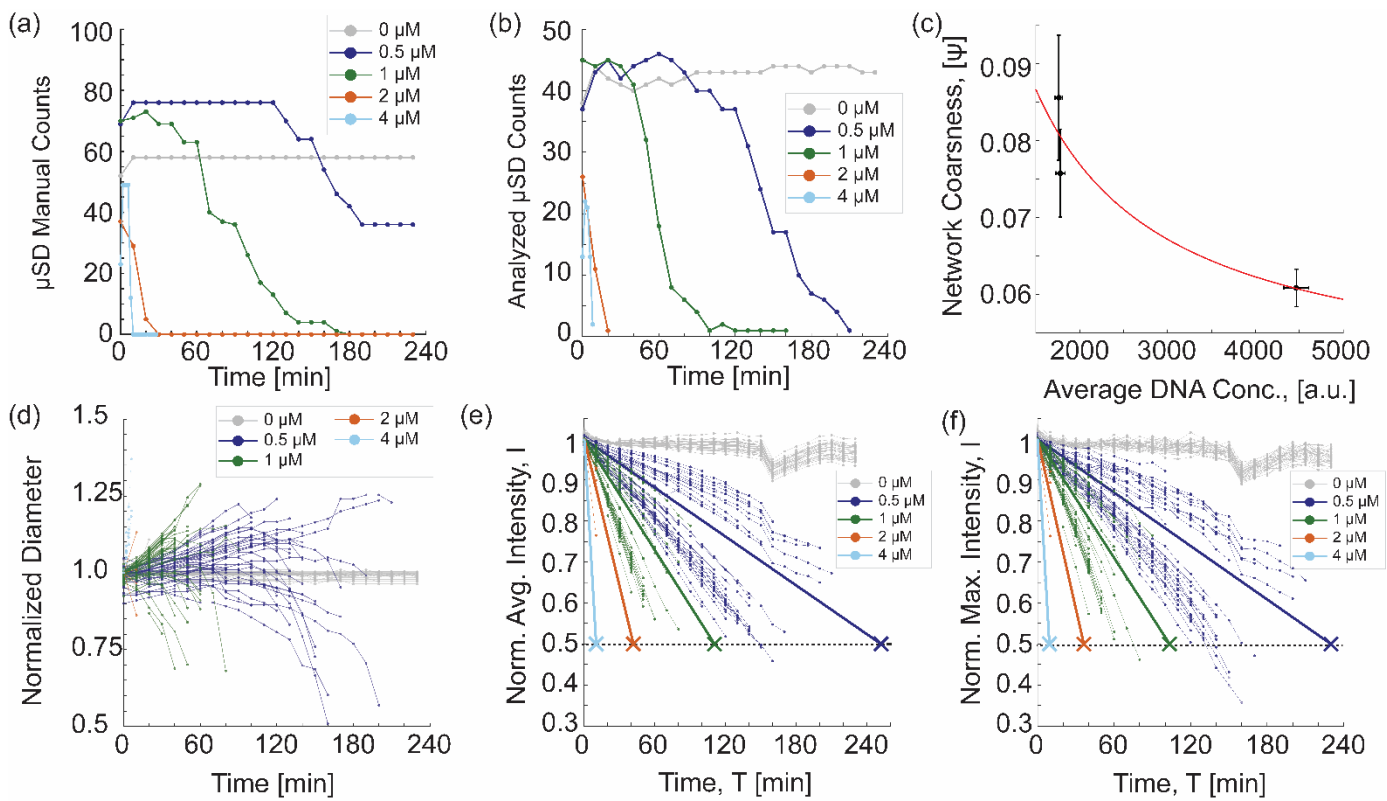


Figure S8: Analysis of μ SD Dissolution Over Time. (a) Raw manual counts of μ SDs in the well plate over time, demonstrating the reduction in hydrogel numbers during dissolution. (b) μ SD counts analyzed using the custom MATLAB code over time. (c) Network coarseness measured in diffusion experiment as a function of average intensity at late time points of 110 to 120 min (average DNA concentration). Plot of network coarseness is inversely related to average DNA concentration with (d) Normalized diameter of μ SDs plotted as a function of time for various concentrations of dissolving strands. (e) Normalized Average Intensity plotted as a function of time (f) Normalized Maximum intensity plotted as a function of time at various dissolving strand concentrations.

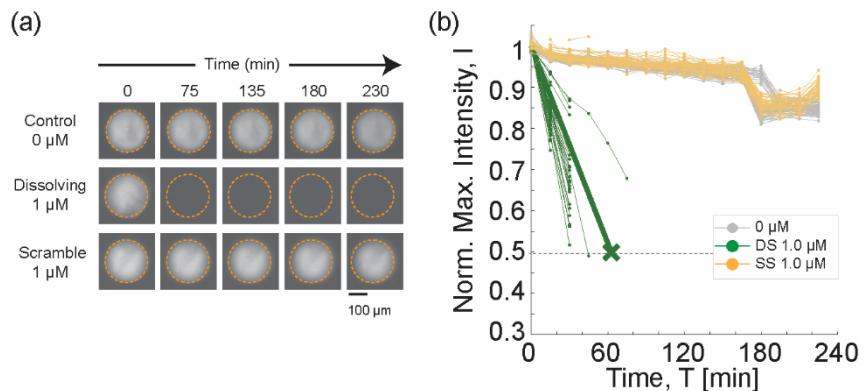


Figure S9: Analysis of μ SD sequence specificity. (a) Sequential images of hydrogels incubated without added DNA strand, with the dissolving strand, and with a scrambled strand. (b) Normalized maximum fluorescence intensity as a function of time for the control, dissolving strand (DS), and scrambled strand (SS).

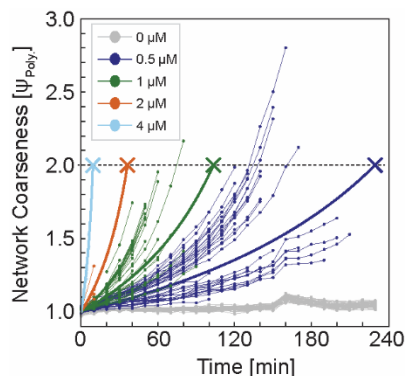


Figure S10: Network coarseness calculated using polymer concentration plotted against time for varying dissolving strand concentrations. Solid lines represent average fitting. The 'x' markers denote the final analyzable timepoints before μ SDs.

Table S1: Diameter comparison of μ SDs in diffusion and swelling experiments.

Condition	Diffusion Data		Swelling Data	
	Mean diameter (μ m) \pm standard error	N	Mean diameter (μ m) \pm standard error	N
Unswell	116.89 \pm 0.38	15	120.9 \pm 0.2	304
2 h swell	152.78 \pm 1.92	6	138.0 \pm 0.5	328
5 h swell	177.04 \pm 1.76	11	155.2 \pm 0.5	297